ARTICLE

View Article Online
DOI: 10.1039/C9TB00909D

Embedding of superparamagnetic iron oxide nanoparticles into membranes of well-defined poly(ethylene oxide)-*block*-poly(ε-caprolactone) nanoscale magnetovesicles as ultrasensitive MRI probes of membrane bio-degradation

Received 7th May 2019,
Accepted 18th June 2019

DOI: 10.1039/C9TB00909D

www.rsc.org/

Adeline Hannecart,[a] Dimitri Stanicki,[a] Luce Vander Elst,[a] Robert N. Muller,[a,b] Annie Brûlet[c], Olivier Sandre,[d] Christophe Schatz,[d] Sébastien Lecommandoux,[d] and Sophie Laurent*[a,b]

The present study reports the preparation of poly(ethylene oxide)-*block*-poly(ε-caprolactone) (PEO-b-PCL) polymer vesicles *via* a nanoprecipitation method and the loading of two different size hydrophobically coated ultrasmall superparamagnetic iron oxide (USPIO) nanoparticles (magnetic core size of 4.2 nm and 7.6 nm) into the membrane of these nanovesicles, whose thickness was measured precisely by small angle neutron scattering (SANS). Spherical nano-assemblies with a high USPIO payload and a diameter close to 150 nm were obtained as confirmed by dynamic light scattering (DLS), transmission electron microscopy (TEM) and cryo-TEM. Vesicular structure of these hybrid nano-assemblies was confirmed by multi-angle light scattering (MALS) measurements. Their magnetic properties were evaluated by T_1 and T_2 measurements (20 and 60 MHz) and by nuclear magnetic relaxation dispersion (NMRD) profiles. The size of USPIO entrapped in the membranes of PEO-*b*-PCL vesicles has a strong impact on their magnetic properties. It affects both their longitudinal and their transverse relaxivities and thus their magnetic resonance imaging (MRI) sensitivity. Acid-catalyzed hydrolysis of PCL membrane also influences their relaxivities as shown by measurements carried out at pH 7 *vs.* pH 5. This property was used to monitor the membrane hydrolytic degradation *in vitro*, as a proof of concept of potential monitoring of a drug delivery by nanomedicines *in vivo* and non-invasively, by MRI.

Introduction

Magnetic resonance imaging (MRI) is currently a leading imaging modality for soft tissues and organs owing to its high spatial resolution, unlimited tissue penetration and non-invasive nature. However, MRI suffers from a low sensitivity and requires in many cases the administration of contrast agents. In this context, the development of MRI contrast agents with great stability and high efficiency is required. The efficiency of a MRI contrast agent is quantified by its longitudinal (r_1) and transverse (r_2) relaxivities, defined as the increases of the proton nuclear relaxation rates $1/T_1$ and $1/T_2$ of the solvent brought by one millimole of magnetically active compound (such as iron or gadolinium) per litre (s^{-1} mM^{-1}). Paramagnetic compounds are used as positive or T_1-contrast agents because they predominantly reduce the longitudinal relaxation time of protons (T_1) and increase the signal where they are present. On the contrary, ultrasmall superparamagnetic iron oxide nanoparticles (USPIO) are effective MRI contrast agents because of their very large magnetic moment. They predominantly reduce the transverse relaxation time of water protons (T_2) and thus decrease the MRI signal intensity. Consequently they are mainly used as negative or T_2-contrast agents [1-3].

Superparamagnetic iron oxide nanoparticles (SPION) can be produced by different synthetic methods carried out either in

[a] *Department of General, Organic and Biomedical Chemistry, NMR and Molecular Imaging Laboratory, University of Mons, 19 avenue Maistriau B-7000 Mons, Belgium*
[b] *Center for Microscopy and Molecular Imaging, 8 rue Adrienne Bolland, B-6041 Charleroi, Belgium*
[c] *Laboratoire Léon Brillouin, CNRS, CEA, Univ. Paris-Saclay, UMR12, F-91191 Gif sur Yvette, France*
[d] *Laboratoire de Chimie des Polymères Organiques, Univ. Bordeaux, CNRS, Bordeaux INP, LCPO, UMR 5629, F-33607 Pessac, France*

Electronic Supplementary Information (ESI) available: Fig. S1: (a) 500 MHz ^{1}H NMR spectrum of PEO_{45}-*b*-PCL_{111} copolymer in $CDCl_3$; (b) chromatogram of PEO_{45}-b-PCL_{111} obtained by GPC; Fig. S2: Plot of the I_{336}/I_{331} ratio against the logarithm of concentration of PEO_{45}-*b*-PCL_{111} suspensions in the presence of pyrene at fixed concentration of 0.6 µM; Fig. S3: TEM image of PEO_{45}-*b*-PCL_{111} polymersomes negatively stained with uranyl acetate (scale bar = 200 nm); Fig. S4: NMRD profiles of the longitudinal relaxivity *vs.* proton Larmor resonance frequency at 37°C for (a) 7.6 nm USPIO and (b) 4.2 nm USPIO; Fig. S5: Size and morphology of PEO_{45}-*b*-PCL_{111} vesicles loaded at 32% FWR with iron oxide nanoparticles of 4.2 nm diameter; Fig. S6: Multi-angle DLS plots: Variations of decay rate Γ versus squared scattering vector q^2 measured by multi-angle DLS; Fig. S7: Multi-angle SLS plots: Guinier (a,b) and Berry (c,d) plots on nanoprecipitated objects made by co-assembly of PEO_{45}-*b*-PCL_{111} with 7.6 nm USPIOs at 16% FWR (a,c) or with 4.2 nm USPIOs at 32% FWR (b,d); Fig. S8: NMRD profiles of the longitudinal relaxivity *vs.* proton Larmor resonance frequency at 37°C for PEO_{45}-*b*-PCL_{111} vesicles loaded at 16% FWR with 7.6 nm USPIOs (circles) and at 32% FWR of 4.2 nm USPIOs (squares); Table. S1: Parameters extracted from the fitted NMRD profiles (D^{NMRD} and M_s^{NMRD}) of USPIOs loaded in PEO_{45}-*b*-PCL_{111} vesicles (in water) and individually dispersed USPIOs (in THF); Fig. S9: Intensity-weighted size distribution measured by DLS of PEO_{45}-*b*-PCL_{111} vesicles measured after synthesis and after magnetic chromatography; Fig. S10: TEM image of PEO_{45}-*b*-PCL_{111} vesicles loaded at 16% FWR with iron oxide nanoparticles of 7.6 nm diameter after magnetic chromatography; Table. S2: Longitudinal (r_1) and transverse (r_2) relaxivities (in water and at 37°C) and resultant r_2/r_1 ratios of USPIO loaded in PEO_{45}-*b*-PCL_{111} vesicles before and after magnetic chromatography; Fig. S11: TEM images (a and b) and intensity-weighted size distributions (c and d) of PEO_{45}-*b*-PCL_{111} vesicles loaded at 16% FWR with 7.6 nm iron oxide nanoparticles: a) and c) sample left 7 days at 37°C and at pH 7 and b) and d) sample left 7 days at 37°C and at pH 5; Fig. S12: Longitudinal relaxivities (a), transverse relaxivities (b) and transverse to longitudinal relaxivitiy ratios (c) at 20 MHz for PEO_{45}-*b*-PCL_{111} vesicles loaded at 16% FWR with 7.6 nm USPIOs at pH 7 (red markers) and pH 5 (blue markers) as function of time. See DOI: 10.1039/x0xx00000x

View Article Online
DOI: 10.1039/C9TB00909D

aqueous or organic media. A commonly used method in aqueous media is the iron salts alkaline coprecipitation but it needs precise adjustment of the experimental conditions and often results into a quite broad particle size distribution. A remarkable non-aqueous process for producing highly magnetized, well crystallized and monodisperse (in size and shape) nanoparticles is the thermal decomposition method [4, 5]. It involves the decomposition of iron complexes in the presence of surfactants (oleic acid, oleylamine,…) in an organic solvent of high boiling temperature (>200°C). However, nanoparticles obtained by this way exhibit a hydrophobic layer and require surface modification to be transferred into aqueous media [6, 7]. In the recent years, several strategies have been developed to modify the nanoparticle surface like ligand addition or ligand exchange [8].

Another interesting way to obtain stable aqueous dispersions from iron oxide nanoparticles synthesized by the thermal decomposition method is their encapsulation via the self-assembly of amphiphilic block copolymers [9]. This approach offers the opportunity to encapsulate several USPIO inside a single nanoplatform, resulting in a significative increase of their MRI sensitivity [10-15]. Moreover, nanocarriers designed by the self-assembly of amphiphilic block copolymers can entrap both imaging and therapeutic agents, extending their applications to the theranostic field. Multifunctional nanocarriers for biomedical applications can therefore be assembled in this way [10, 15, 16]. As shown by Lecommandoux *et al.* [17], two main morphologies can be produced by the self-assembly of amphililic copolymers with USPIO: magnetomicelles and magnetovesicles (*i.e.* magnetic polymersomes). While micelles are generally formed by the self-assembly of amphiphilic copolymers presenting a large hydrophilic part, vesicles are formed with block copolymers presenting a large hydrophobic part [18]. A parameter used to predict the morphology of the self-assembled system is the volume fraction of the hydrophilic block (*f*). As a rule of thumb, for PEO-based block copolymers, copolymers with f_{EO} greater than 0.45 will usually induce the formation spherical micelle, while those with $0.40 > f_{EO} > 0.20$ will progressively form worm-like micelles and then vesicles for the lowest hydrophilic fractions [19, 20]. Although the hydrophilic block fraction is an important parameter, the final morphology and size also depend on the crystallinity of the copolymer, and the experimental conditions used during the self-assembly process (temperature, addition of solvent into water or the reverse, mixing rate etc…).

Polymersomes are attractive nanocarriers because they can load hydrophilic as well as hydrophobic compounds in their aqueous lumen and membrane, respectively [21-26]. In contrast to their lipid counterparts (liposomes), they possess thicker membranes which make them more robust and facilitate the incorporation of hydrophobic nanoparticles [27]. Indeed, the inclusion of hydrophobic nanoparticles into liposome membranes can be difficult because these nanoparticles are usually larger than the hydrophobic bilayer which is typically 3-4 nm thick [28].

Several studies have reported the formation of poly(ethylene oxide)-*block*-poly(ε-caprolactone) (PEO-*b*-PCL) based vesicles, which are predominantly formed when f_{EO} is between 12 and 28 % [29-38]. Among the different PEO-*b*-PCL formulations screened, compositions close to PEO_{45}-*b*-PCL_{105} (where 45 and 105 refer to the respective average degree of polymerization of each monomer unit) have been widely reported to form vesicles [29, 30, 32, 34, 35]. PEO-*b*-PCL polymersomes possess a high potential for biomedical applications. PEO block is biocompatible and its presence on the surface of nanoparticles reduces their non-specific interactions with plasma proteins which decrease their opsonization and increases their blood plasma circulation time. On the one hand, polymer vesicles made from PEO-based copolymers have been shown to remain intact and circulate for more than one day in rats [35]. On the other hand, PCL block is biodegradable and the hydrolysis of its ester linkages is accelerated in an acidic medium providing a controlled release of drugs at acidic pH [29, 35]. Until now, studies on PEO-*b*-PCL vesicles mainly focused on their preparation and characterization methods and/or on the loading and release of drugs. However, to the best of our knowledge, no work has be done on the encapsulation of hydrophobically coated USPIOs into these nano-assemblies produced from PEO-*b*-PCL copolymers with long PCL blocks.

In the present work, USPIOs possessing two different sizes (D_{TEM} = 4.2 nm and D_{TEM} = 7.6 nm) were synthesized by the thermal decomposition method and their encapsulation into the membranes of PEO_{45}-*b*-PCL_{111} polymer nanovesicles is reported. Magnetopolymersomes obtained in this study are characterized by very large r_2/r_1 ratios (at 20 and 60 MHz), which makes them highly promising canditates as T_2-contrast agents for MRI. The effect of the size of the membrane-embedded iron oxide nanoparticles on r_1 and r_2 relaxivities was studied. Furthermore, we demonstrated for the first time *in vitro* that PCL hydrolysis in magnetopolymersome membranes significantly affects their magnetic relaxation properties, illustrating their potential to monitor PCL membrane degradation *in vivo*, which opens very promising possibilities for image-guided anti-cancer nanotherapies.

Experimental

Materials.

Iron(III) acetylacetonate $Fe(acac)_3$ (97%), oleic acid (90%), oleylamine (70%), benzylether (99%), tetrahydrofuran (> 99%), pyrene (> 99%) and iron standard for ICP (1000 ppm) were purchased from Sigma-Aldrich (Bornem, Belgium) and used as received. 1,2-hexadecanediol (> 98%) and oleyl alcohol (> 60%) was provided by TCI (Zwijndrecht, Belgium). Ethanol (100%) was purchased from Chem-Lab (Zedelgem, Belgium).

Synthesis of iron oxide nanoparticles.

Iron oxide nanoparticles were synthesized by the thermal decomposition method with the use of iron (III) acetylacetonate ($Fe(acac)_3$) as the organometallic precursor. Two different organic solvents were used in order to get USPIO with two

10.1039/C9TB00909D

different sizes, namely dibenzyl ether and a mixture of oleyl alcohol/dibenzyl ether (50 :50).

Synthesis of 7.6 nm iron oxide nanoparticles. Briefly, 1, 2-hexadecanediol (10 mmol, 2.58 g), oleic acid (2 mmol, 636 µL) and oleylamine (2 mmol, 658 µL) were added to dibenzyl ether (10 mL) in a three-neck round-bottom flask under magnetic stirring and a nitrogen atmosphere. This mixture was heated to 300°C before the rapid injection of an iron precursor solution: $Fe(acac)_3$ in dibenzyl ether (706 mg in 10 mL, 2 mmol). The reaction mixture was kept under heating at 300°C under magnetic stirring and nitrogen atmosphere for 30 minutes. After cooling down to room temperature, 40 mL of ethanol was added to the mixture and the black precipitate was isolated by magnetic decantation. The precipitate was then washed three times with ethanol. Finally, nanoparticles were dispersed in 40 mL of tetrahydrofuran (THF) and the solution was centrifuged (16000 g, 30 minutes) to remove any undispersed material.

Synthesis of 4.2 nm iron oxide nanoparticles. 4.2 nm iron oxide nanoparticles were synthesized by using a mixture of oleyl alcohol/dibenzyl ether (50:50) instead of dibenzyl ether as reaction solvent. 1, 2-hexadecanediol (10 mmol, 2.58 g) and oleylamine (2 mmol, 658 µL) were added to oleyl alcohol (10 mL) in a three-neck round-bottom flask under magnetic stirring and a nitrogen atmosphere. This mixture was heated to 300°C before the rapid injection of the iron precursor solution (2 mmol, 706 mg of $Fe(acac)_3$ dissolved in dibenzyl ether (10 mL)). The reaction mixture was kept under heating at 300°C under magnetic stirring and a nitrogen atmosphere for 30 minutes. The black-coloured mixture was then cooled down to room temperature. Following the workup procedures described in the synthesis of 7.6 nm nanoparticles, a black-brown THF dispersion of 4.2 nm Fe_3O_4 nanoparticles was produced.

Self-assembly of PEO_{45}-*b*-PCL_{111} copolymer.

PEO_{45}-*b*-PCL_{111} was synthesized by ring opening polymerization (ROP) of ε-caprolactone (CL) monomer in the presence of methyl-PEO-OH macroinitiator [40]. Nanoprecipitation of PEO_{45}-*b*-PCL_{111} copolymer was carried out by dissolving the polymer (10 mg) in THF (500 µL). Deionized water (9 mL) was then added instantaneously to the THF solution under magnetic stirring at room temperature. The mixture was kept under stirring for 15 minutes. THF was removed from the aqueous solution by dialysis against deionized water (MWCO: 12000-14000 $g{\cdot}mol^{-1}$). Samples were finally sized down by extrusions repeated an odd number of times at 60°C through polycarbonate (PC) filters of diameter from 1 µm down to 100 nm using a thermally controlled steel cylinder connected to pressurised nitrogen gas.

Self-assembly of PEO_{45}-*b*-PCL_{111} with iron oxide nanoparticles.

USPIO-embedding polymersomes were prepared by co-assembly using the same nanoprecipitation method. Hydrophobically coated iron oxide nanoparticles at a concentration in THF (500 µL) in a predetermined feed weight ratio (FWR) with polymer were mixed with PEO_{45}-*b*-PCL_{111} copolymer (10 mg). Deionized water (9 mL) was then added under magnetic stirring at room temperature. The mixture was kept under stirring for 15 minutes. Subsequently, THF was eliminated from the suspension by dialysis against deionized water (MWCO: 12000-14000 $g{\cdot}mol^{-1}$). The suspension was finally gently centrifuged to remove any agglomerates and then downsized by an odd number of extrusion steps at 60°C through PC membranes using a thermally controlled steel cylinder connected to pressurized nitrogen gas.

Evidence of the PEO_{45}-*b*-PCL_{111} acidolysis

Magnetovesicle suspensions (encapsulating 7.6 nm USPIOs at 16% FWR) were left at 37°C at pH 5.2 (Sorensen buffer) or at pH 7.4 (PBS buffer) for a period of one week. Relaxation times were determined at regular intervals on aliquots.

Similarly, empty-vesicle suspensions were left at 37°C at pH 5.2 (Sorensen buffer) or at pH 7.4 (PBS buffer) for a period of one week. Aliquots taken at different times (24, 72, 144, 168, 208 hours) were lyophilized and the resulting residues were purified by dialysis against deionized water (MWCO: 100-500 $g{\cdot}mol^{-1}$) before lyophilisation and GPC analysis in THF.

Magnetic chromatography.

Magnetovesicle suspensions were deposited onto a magnetic separation column (LS column™, Miltenyi Biotec, Leiden, The Netherlands) placed in a magnet. The retained vesicles were washed with deionized water and then retrieved after removal of the magnet and elution with deionized water.

Critical aggregation concentration (CAC) determination.

The CAC of the copolymer in aqueous medium was determined by a fluorescence technique using pyrene as a nonpolar probe. Pyrene solution in acetone (4.8×10^{-5} M, 50 µL) was added to 4 mL of aqueous polymer solutions at different concentrations. The obtained samples were stirred for 48 h at room temperature to allow evaporation of acetone. The resulting samples possess a constant pyrene concentration of 0.6 µM. Fluorescence spectra were recorded on a spectrofluorometer (LS 55, PerkinElmer, Waltham (MA), USA) at a scanning rate of 50 nm/min at room temperature; the slit widths were set at 2.5 nm. Excitation spectra of pyrene were recorded in the range 300-360 nm with the emission wavelength set at 371 nm. The CAC was estimated as the cross point of straight lines obtained at low and high concentration regions by plotting the intensity ratio I_{336}/I_{331} against the logarithmic concentration of the copolymer [41].

Instrumentation.

Dynamic light scattering (DLS) measurements were conducted at 20°C on a Zetasizer NanoZS ZEN 3600 instrument (Malvern, UK) to measure the hydrodynamic diameters (D_H) and polydispersity index (PDI^{DLS}). Reported D_H and PDI^{DLS} values were measured in triplicate from the 2nd order cumulant fit of the correlograms obtained from the backscattered light intensity at 173° scattering angle.

Multi-angle DLS and static light scattering (SLS) studies were performed with an ALV/CGS-3 compact laser goniometer equipped with a 632.8 nm HeNe laser (4 mW) and an ALV-5000/EPP multi tau digital correlator. Measurements were

View Article Online
DOI: 10.1039/C9TB00909D

ARTICLE

carried out over an angle range from 40° to 140° in 10° stepwise increments. A cylindrical glass cell containing 1 mL of the sample was immersed in a filtered toluene bath, whose background signal was measured at all angles for Rayleigh ratio determination. Refractive index increment (d*n*/d*c*) was determined with a gel permeation chromatography (GPC) system equipped with a refractometer detector. Suspensions of copolymer co-assembled with IONPs at constant FWR and different total concentrations *c* were analysed and a linear fit yielded the value of d*n*/d*c*. For multi-angle DLS experiments, the CONTIN fit introduced by Provencher [42] was applied on the autocorrelograms to obtain the decomposition into decay rate modes Γ_i without any assumption on their number. Then Γ_i values were plotted *versus* the square of the light scattering vector $q=4\pi n\sin(\theta/2)/\lambda$ where *n* is the solvent refraction index, λ the wavelength and θ the scattering angle in order to get the corresponding translational diffusion constants, converted into hydrodynamic diameters using Stokes-Einstein's relationship.

Transmission electron microscopy (TEM) images were recorded on a Microscope Fei Tecnai 10 operating at an accelerating voltage of 80 kV (Oregon, USA). For USPIO samples, a drop of diluted suspension ([Fe] ≈ 0.5 mM) in THF was placed on a carbon-coated copper grid (300 mesh). Images were analysed using automated particle counting of ImageJ software after thresholding and watershed filtering, enabling to perform a statistical treatment of the diameters. Based on a minimum of 1000 nanoparticles per batch, the polydispersity index (PDI^{TEM}) was calculated using the following equations, by analogy with dispersity (Đ) defined for polymer chains, but subtracting 1 to obtain a PDI below 1 (like in DLS):

$$PDI^{TEM} = \frac{\overline{D_w}}{\overline{D_n}} - 1$$

$$\text{where } \overline{D_n} = \frac{\sum_i n_i D_i}{\sum_i n_i} \text{ and } \overline{D_w} = \frac{\sum_i n_i D_i^4}{\sum_i n_i D_i^3} \quad (1)$$

$\overline{D_n}$ and $\overline{D_w}$ are the number-average and the weight-average diameters, respectively, and n_i the number of nanoparticles of diameter D_i.

For empty vesicles (pure PEO-*b*-PCL nanoprecipitated copolymer), negatively stained TEM images were acquired by placing successively a drop of diluted suspension (2 minutes), a drop of phosphate-buffered saline (pH 7.4) (2 minutes), a drop of DI water (2 minutes) and a drop of uranyl acetate 2% (w/v) solution (10 minutes) on a carbon-coated copper grid (300 mesh). Surplus of solutions were removed before each grid transfer. TEM images of vesicles loaded with USPIOs were obtained on grids prepared by placing a drop of diluted suspension ([Fe] ≈ 0.1 mM) on a Formvar™-coated copper grid (300 mesh).

Cryo-TEM images were recorded at the Institut de Physique et Chimie des Matériaux of Strasbourg (IPCMS, Pr. O. Ersen and D. Ihiawakrim) on a Microscope JEOL 2100 F operating at an accelerating voltage of 200 kV. A drop of diluted suspension was placed on a carbon-coated copper grid (300 mesh), which was beforehand treated with an ELMO glow discharge unit (Cordouan Technologies, Pessac, France) to render the surface hydrophilic. The drop size was reduced with a filter paper until having a thin film. The grid was then plunged into liquid nitrogen and subsequently in liquid ethane. Maintained at a temperature near liquid nitrogen temperature (-190°C), the grid was transferred to a cryo-holder which was introduced into the high-vacuum column of the microscope.

Small angle neutron scattering (SANS) measurements were performed on the PACE spectrometer of Laboratoire Leon Brillouin (CEA-Saclay, France). Three configurations were used by varying the sample to detector distance and the neutrons wavelength (λ) in order to cover a large q range: $3.18\ 10^{-3}$ – $3.70\ 10^{-1}$ A^{-1}. The samples were prepared in pure heavy water (pure copolymer) or in a mixture of 20% v/v D_2O and H_2O, matching the theoretical neutron scattering length density (SLD) of the PCL blocks for those loaded with iron oxide NPs, in quartz cuvettes of respective thicknesses 2 mm or 1 mm. The scattering curves were divided by the transmission factor and by the thickness after subtracting the signal of an empty cuvette. Correction of the efficacy of the detector was performed by normalizing the curves by the signal of a 1 mm cuvette filled with light water to obtain the scattering intensity, *I(q)*, in absolute value (cm^{-1}) [43].

Dosage of iron was performed by Inductively Coupled Plasma-Atomic Emission Spectroscopy (ICP-AES) on a Jobin Yvon JY70C instrument (Longjumeau, France). The total amount of iron was determined after microwave digestion (Milestone MLS-1200 MEGA, Gemini B.V., Apeldoorn, the Netherlands) in a mixture of nitric acid (600 µL, 65 %) and hydrogen peroxide (300 µL, 35%). An iron standard solution for ICP (1000 mg·mL^{-1} of iron in nitric acid) was used to obtain a calibration curve (linear correlation coefficient = 0.99).

Molecular weight distribution of the copolymers was measured by gel permeation chromatography (GPC) analysis (Agilent 1200 apparatus) equipped with a differential refractive index detector. Sample solutions (1 mg/mL in THF, 2% NEt_3) were injected with a 1 mL·min^{-1} flow rate at 35°C, in a pre-column PLgel 10 µm (50 × 7.5 mm) and in two gradient columns PLgel 10 µm mixed-B (300 × 7,5mm) (Laboratory of Polymeric and Composite Materials, Pr. P. Dubois, UMonS). Additional GPC analyses of PCL block hydrolysis as a function of time and pH were performed with THF as eluent on an UltiMate 3000 system from Thermo Fisher Scientific equipped with a diode array detector (DAD), a multi-angle light scattering (MALS) detector and a differential refractive index (dRI) detector from Wyatt Technology Corp. (Toulouse, France). Polymers were separated on three G2000, G3000 and G4000 TOSOH HXL gel columns (300 × 7.8 mm) (size exclusion limits from 1000 to 400 000 g·mol^{-1}) held at 40°C and under a THF flowrate of 1 mL/min. EasiVial™ kit of Polystyrene from Agilent was used as the M_n calibration standard (from 162 to 364 000 g·mol^{-1}).

Nuclear magnetic resonance (NMR) spectrum was recorded on a Bruker Avance 500 MHz spectrometer (Karlsruhe, Germany). DOSY-NMR measurements were conducted using a

Author version of manuscript accepted for publication

10.1039/C9TB00909D

STE-LED (stimulated echo-longitudinal eddy current delay) standard sequence with a diffusion time (Δ) of 250 ms, a gradient pulse length (δ) of 1 ms and 16 gradients ranging from 2% to 95% of the maximum gradient (53 G/cm).

Nuclear magnetic relaxation dispersion (NMRD) profiles reporting the longitudinal relaxation rates of water protons (R_1) over a magnetic field range from 0.25 mT to 0.94 T (0.015 - 40 MHz proton resonance frequency) were recorded on a Fast Field Cycling (FFC) relaxometer (Stelar, Mede, Italy). The apparent saturation magnetization (M_S^{NMRD}), the Néel relaxation time (τ_N) and size of superparamagnetic crystal (D^{NMRD}) were determined by fitting these NMRD curves numerically with the MINUIT minimisation program within the frame of the Outer Sphere relaxation model and a standard phenomenological approximation [40]. Additional longitudinal (T_1) and transverse (T_2) relaxation times were measured at 37°C on Bruker Minispec mq20 and mq60 relaxometers working respectively at 20 MHz (0.47 T) and 60 MHz (1.41 T). The diamagnetic contributions of THF to the relaxation rates at 37°C are R_1 = 0.2759 s^{-1} and R_2 = 0.2984 s^{-1} at 20 MHz and R_1 = 0.2227 s^{-1} and R_2= 1.4837 s^{-1} at 60 MHz.

Results and discussion

Characterization and self-assembly of PEO_{45}-*b*-PCL_{111} copolymer.

A copolymer of PEO-*b*-PCL was synthesized by ring opening polymerization of ε-CL monomer initiated by PEO chains with M_n of 2000 g·mol^{-1} possessing two different end-groups, respectively $-CH_3$ and –OH. The chemical structure of PEO-*b*-PCL copolymer was assessed by ^1H NMR spectroscopy. The ^1H NMR spectrum shows typical peaks of PEO-*b*-PCL copolymers, whose integral intensities were used to determine the composition of the PEO-*b*-PCL copolymer (Fig. S1a in supporting information). The final block copolymer composition is PEO_{45}-*b*-PCL_{111}, where 45 and 111 are the respective average degrees of polymerization (DP) of each monomer unit. This composition is close to the target hydrophilic ratio (14% weight fraction) of PEO_{45}-*b*-PCL_{105}, which was chosen owing to its tendency to form a vesicular morphology [29, 30, 32, 34, 35, 37]. The copolymer is characterized by a relatively wide molecular weight dispersity (Đ=M_w/M_n = 1.35) as indicated by GPC (Fig. S1b in supporting information). In this work, we opted for a fast, efficient and easy to implement method for the formation of the nano-assemblies, i.e. by the solvent shift method, also called nanoprecipitation. Sequential extrusions at 60°C (*i.e.* above the melting curve of PCL) through 1 µm, 0.8 µm, 0.4 µm and 0.2 µm pore size filters were necessary to narrow the size distribution (Fig. 1). TEM experiments (Fig. S3 in supporting information) confirm the formation of 60 nm diameter spherical nanostructures, suggesting thus the formation of the expected vesicles.

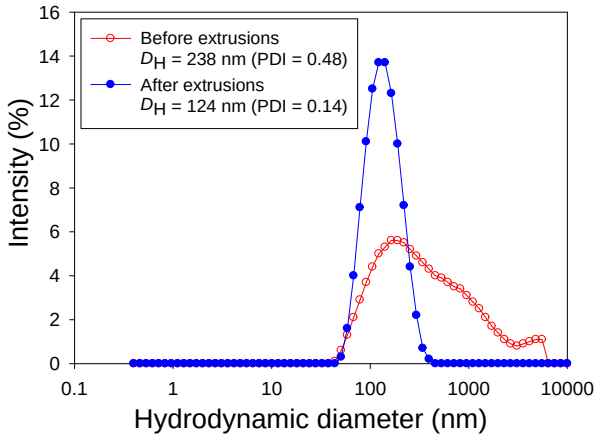

Figure 1. Intensity-weighted size distributions of PEO_{45}-*b*-PCL_{111} suspensions obtained by the nanoprecipitation method before (empty circles) and after (filled circles) extrusions through 1 µm to 0.2 µm pore size filters.

SANS experiments were performed on PEO_{45}-*b*-PCL_{111} self-assemblies in order to confirm their vesicular structures and estimate their membrane thicknesses. SANS curves were fitted with the vesicle (shell) form factor thanks to SASView software. The values obtained from the fitting are R_{in} = 84 nm and d = 17 nm, where R_{in} corresponds to the inner aqueous compartment radius and d to the membrane thickness (the radius of the vesicle R_{tot}, is given by: $R_{tot} = R_{in} + d$). One can note that radii and thickness values calculated by fitting the SANS curves exhibit broad dispersity parameters σ (no unit),e as samples analysed by SANS were not extruded to avoid sample loss on the filters as SANS analysis requires concentrated enough samples, in this case 6.2 mg·mL^{-1}). The *I(q)* curves computed using a hollow spherical shell model are well superimposed on experimental data, supporting the assumption that nano-vesicles are formed through the self-assembly of PEO_{45}-*b*-PCL_{111} copolymers (Fig. 2).

In the intermediate range of scattering vectors, the neutron scattering intensities vary as q^{-2}, this scaling law being characteristic of vesicular structures that exhibit locally planar morphology. The Kratky-Porod plot (ln [I(q)q^2] *versus* q^2) enables accessing the membrane thickness (d) with more robustness than a fit thanks to the following asymptotic law [45]:

$$\ln\left[I(q)q^2\right] \cong \left(\frac{-q^2d^2}{12}\right) \qquad (2)$$

Ln [$I(q)q^2$] plotted *versus* q^2 in figure 2 enables deducing a membrane thickness of 21 nm from the slope. Noteworthy, a membrane thickness of 22.5 nm was reported for PEO_{45}-*b*-PCL_{105} vesicles in the literature (measured by cryo-TEM analysis) [29], in good agreement with the value determined by SANS in the present study. The critical aggregation concentration (CAC) of PEO_{45}-*b*-PCL_{111} copolymer in aqueous medium was determined by the fluorescence technique using pyrene as a probe sensitive to a nonpolar environment (at fixed concentration of 0.6 µM). As the block copolymer concentration increases, a shift of the band from 331 to 336 nm was observed: then by plotting the I_{336}/I_{331} ratio (from the excitation spectra)

ARTICLE DOI: 10.1039/C9TB00909D

against the logarithm of the concentration (Fig. S2 in supporting information) a break is observed corresponding to the value of log (CAC). This low CAC value of 1.4 µg·mL^{-1} indicates a good stability of PEO_{45}-*b*-PCL_{111} vesicles upon dilution.

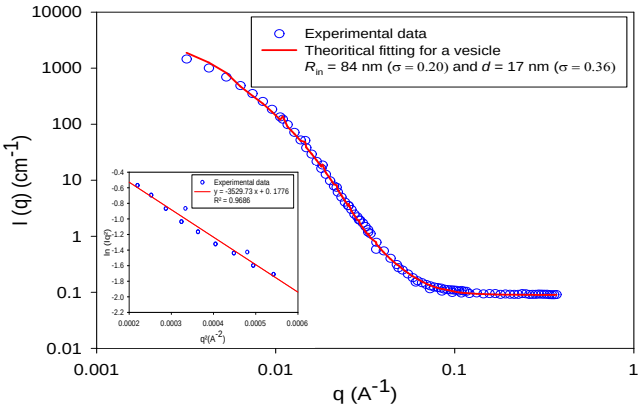

Figure 2. SANS curves of PEO_{45}-*b*-PCL_{111} vesicles: experimental data are plotted as open circles while solid lines represent the simulated intensity considering the form factor of hollow spheres with log-normal distributions on both R_{in} and *d*, whose standard values (σ) are indicated. The insets shows the representation of ln[$I(q)q^2$] *versus* q² calculated from SANS measurements in the Kratky-Porod regime giving a membrane thickness of 21 nm.

Iron oxide nanoparticles having two different sizes (4.2 nm and 7.6 nm) were synthesised by the thermal decomposition method. Narrow size distributions typical of this synthesis procedure were obtained. TEM images of USPIO were used to determine the size distribution of the magnetic cores (Fig. 3). The average diameters (D^{TEM}) and the polydispersity index (PDI^{TEM}) extracted from a statistical treatment of sizes measured on TEM images as well as hydrodynamic diameters (D_H) and PDI measured by DLS (PDI^{DLS}) using the 2nd order Cumulant fit of correlograms are reported in Table 1. NMRD profiles which display the evolution of proton longitudinal relaxivity r_1 as a function of the applied field (or the corresponding proton resonance frequency) were recorded on these two samples (Fig. S4 in supporting information). These profiles were fitted using the usual Outer Sphere theory modelling the acceleration of proton relaxation induced by superparamagnetic NPs [44] applied to suspensions in THF, for which a molecular diffusion coefficient of 3.27 10^{-9} cm²·s^{-1} at 37°C has been measured independently by diffusion-ordered NMR spectroscopy (DOSY). Table 1 shows the values of the relaxometric Outer Sphere diameter (D^{NMRD}), which represents the shortest distance between the centre of the magnetic core of the USPIOs and the THF molecules, together with their apparent saturation magnetization (M_s^{NMRD}) values that are almost identical (~ 50 A·m²·kg^{-1}) for both samples.

Characterization of iron oxide nanoparticles.

Table 1. Physicochemical characteristics of the USPIOs synthesised by the thermal decomposition method: diameter measured by TEM, DLS, NMRD, saturation magnetization (M_s^{NMRD}) and Néel relaxation time (τ_N) extracted from the fits of NMRD profiles.

Sample	D^{TEM} (nm)	PDI^{TEM}	D_H (nm)	PDI^{DLS}	D^{NMRD} (nm)	M_s^{NMRD} (A·m²·kg^{-1})	τ_N (ns)
7.6 nm USPIO	7.6	0.14	11.8	0.05	8.5	49.4	2.24
4.2 nm USPIO	4.2	0.08	8.4	0.03	5.6	49.7	2.69

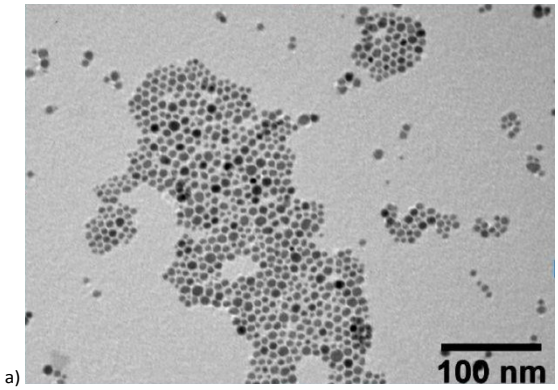

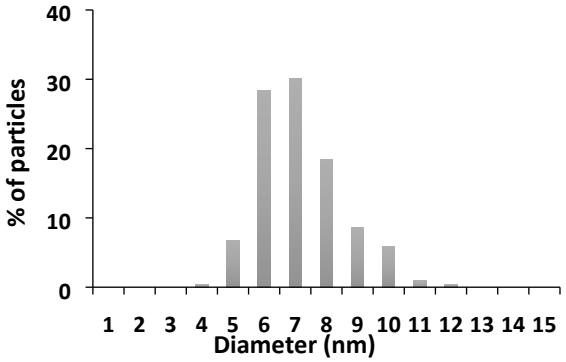

Author version of manuscript accepted for publication

DOI: 10.1039/C9TB00909D

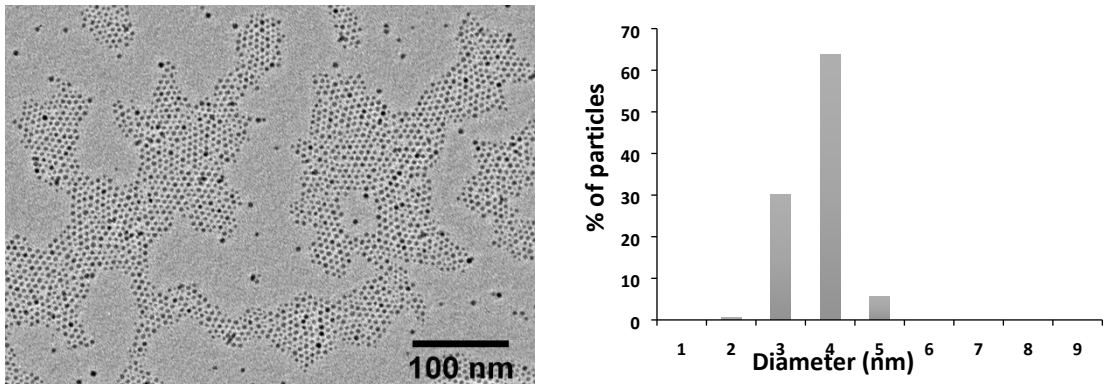

Figure 3. TEM images and histogram of diameters of USPIO synthesized by the thermal decomposition method: (a) USPIO with D^{TEM} = 7.6 nm (7.6 ± 1.6 nm, PDI^{TEM} = 0.14) and (b) USPIO with D^{TEM} = 4.2 nm (4.2 ± 0.5 nm, PDI^{TEM} = 0.08). PDI values are defined by Eq. (1).

Longitudinal (r_1) and transverse (r_2) relaxivities were measured in THF (37°C) at 20 and 60 MHz. Iron oxide nanoparticles with larger diameters possess higher longitudinal and transverse relaxivities and higher transverse to longitudinal relaxivity ratios, while staying at low values (r_2/r_1 below 3) typical for small and well-dispersed (un-aggregated) USPIOs (Table 2).

Table 2. USPIO's longitudinal and transverse relaxivities measured at 20 and 60 MHz (in THF and 37°C) and resultant r_2/r_1 ratios.

Sample	Frequency (MHz)	r_1 (s^{-1} mM^{-1})	r_2 ($s^{-1}mM^{-1}$)	r_2/r_1
7.6 nm USPIO	20	21.9	36.6	1.7
	60	12.8	37.7	2.9
4.2 nm USPIO	20	8.6	12.1	1.4
	60	7.8	17.9	2.3

Formulation and characterization of USPIO loaded in PEO_{45}-*b*-PCL_{111} polymersomes

Nanoprecipitation of PEO_{45}-*b*-PCL_{111} co-assembled with iron oxide nanoparticles was performed by varying the initial USPIO concentration at constant copolymer concentration, the ratio of their weight concentrations in THF being defined as the "feed weight ratio" (FWR). After adjustment, the best results were obtained by mixing 10 mg of the block copolymer with 500 µL of THF containing USPIOs at concentrations close to $[Fe]_0$ ~ 40 mM for 7.6 nm USPIO and $[Fe]_0$ ~ 80 mM for 4.2 nm USPIO. The corresponding FWR values are respectively 16% and 32%, within the same range as in the study by Arosio *et al.* [46] with another amphiphilic copolymer also forming vesicles. Above these threshold values, no more USPIOs could be entrapped in the vesicle membranes and large aggregates of USPIOs were observed by mere visual inspection. The TEM image of the sample obtained by nanoprecipitation of PEO_{45}-*b*-PCL_{111} loaded at 16% FWR with 7.6 nm USPIO shows spherical structures with a high USPIO content as well as some filamentous fragments connected to some of the spheres certainly formed during the drying step of the TEM grid preparation (Fig. 4a). To confirm that these fragments arise from the destruction of spherical structures during the drying step, cryo-TEM imaging allowing the visualization of colloids in the frozen-hydrated state was performed. As expected, only spherical structures were observed (Fig. 4b). However, it can be noted that these spherical structures are arranged into chain-like aggregates, which could be an artefact due to their accumulation within the wedge of the ultrathin frozen film near a border of the TEM grid (being sterically excluded from the centre of the film because its thickness becomes smaller than vesicles diameter). The absence of clusters in the liquid suspensions is confirmed by dynamic light scattering measurements showing a monomodal size distribution with a mean hydrodynamic diameter close to 130 nm (D_H = 129 nm, PDI^{DLS} = 0.13) (Fig. 4c), characteristic of well-defined and individually dispersed objects.

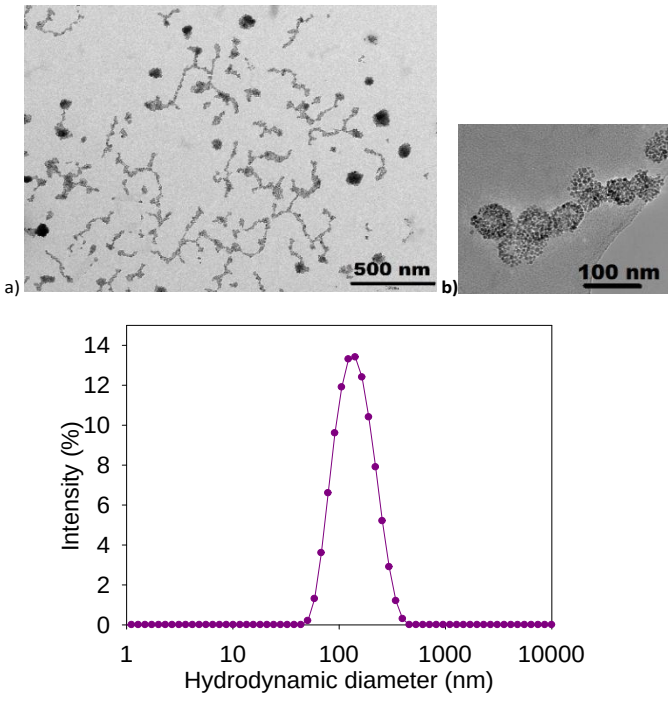

Figure 4. Size and morphology of PEO_{45}-*b*-PCL_{111} vesicles loaded at FWR=16% with USPIO nanoparticles of 7.6 nm diameter. (a) Low magnification TEM image showing intact spherical structures as well as some fragments (scale bar = 500 nm). (b) Cryo-TEM image showing only spherical structures (scale bar = 100 nm). (c) Intensity-weighted size distribution measured by DLS (D_H = 129 nm, PDI^{DLS} = 0.13).

ARTICLE DOI: 10.1039/C9TB00909D

Nanoprecipitation of PEO_{45}-*b*-PCL_{111} loaded at 32% FWR with 4.2 nm USPIO gave similar results. Spherical structures exhibiting a high USPIO content were observed on the TEM images (Fig. S4a in supporting information). A mean hydrodynamic diameter of 146 nm (PDI^{DLS} = 0.10) was measured by DLS (the intensity-weighted size distribution is given in Fig. S4b). Concerning vesicle stability on time, the size distribution of magnetovesicles did not change significantly after storage for one month at 4°C. Multi-angle dynamic (DLS) and static (SLS) light scattering measurements were conducted on nanoprecipitated samples obtained by co-assembly of PEO_{45}-*b*-PCL_{111} with USPIOs of both sizes. Mean values of the radius of gyration (R_G), aggregate weight-averaged molar mass (M_w^{agg}) and aggregation number, i.e. the number of macromolecules per aggregates (*Z*), were determined from SLS measurements upon drawing Guinier and Berry plots (at several weight concentrations and over a scattering angular range of 40-140°). These plots are provided in Supporting Information (Fig. S5 and Fig. S6). The determination of the refractive index increment d*n*/d*c* as measured using a RI detector for GPC was required to determine the molar masses of the self-assembled nanostructures. Resulting d*n*/d*c* values were 0.102 $L{\cdot}g^{-1}$ for PEO_{45}-*b*-PCL_{111} loaded at 16% FWR with 7.6 nm USPIOs and 0.147 $L{\cdot}g^{-1}$ for PEO_{45}-*b*-PCL_{111} loaded at 32% FWR with 4.2 nm USPIOs. Such increase of the RI increment when inorganic NPs like USPIOs (whose RI is ~2.3) are embedded in the objects was predictable. As the mean value hydrodynamic radius can depend on the scattering angle used for the measurement (as ascribed to size dispersity), multi-angle DLS measurements were performed over the same scattering angle range to measure the angle-average hydrodynamic radius (R_H). From these measurements, one can calculate the ratio $\rho = R_G/R_H$, which enables to estimate the morphology of the self-assembly nanostructures: vesicles are characterized by ρ values close to 1 while ρ values around $\sqrt{(3/5)} \approx 0.775$ are expected for spherical micelles [47, 48]. In the present study, the ρ values calculated from the experimental multi-angle DLS and SLS results are in good agreement with vesicular structures (Table 3). Although they appear a bit higher, the *Z* values ~ $5\text{-}7{\cdot}10^4$ calculated for the aggregation numbers of copolymers (after subtracting the fraction of mass of iron oxide in the objects) are also in agreement with values $Z \sim 3{\cdot}10^4$ reported by Adams *et al.* [26] for polymersomes made of PEO_{45}-*b*-PCL_{101}. In conclusion, nano-objets produced by the self-assembly of PEO_{45}-*b*-PCL_{111} with hydrophobically coated USPIOs are vesicles possessing a diameter close to 160-180 nm. These nanoprecipitated objects remain of vesicular morphology, despite their high USPIO payload (16 or 32% FWR) that can fit within the thick hydrophobic membranes.

Table 3. Structural characteristics of PEO_{45}-*b*-PCL_{111} magnetovesicles measured by multi-angle DLS and SLS measurements: Hydrodynamic radius R_H measured by decay rate plots *vs.* square of scattering vector (Fig. S5a,b), radius of gyration R_G measured from Guinier plots (Fig. S6a,b), molar mass of scatterers M_w^{agg} and aggregation number $Z = M_w^{agg}/(1+FWR)/M_w^{polymer}$ of the constituting macromolecules deduced from Berry plots (Fig. S6c,d).

Sample	R_H (nm)	R_G (nm)	$\rho = R_G/R_H$	M_w^{agg} ($g{\cdot}mol^{-1}$)	*Z*
PEO_{45}-*b*-PCL_{111} +7.6 nm USPIO at 16% FWR	92.0	89.2	0.97	$1.9\ 10^9$	$7{\cdot}10^4$
PEO_{45}-*b*-PCL_{111} + 4.2 nm USPIO at 32% FWR	90.3	81.5	0.91	$1.7\ 10^9$	$5{\cdot}10^4$

Relaxometric properties of USPIOs loaded in PEO_{45}-*b*-PCL_{111} vesicles.

An MRI contrast agent is a magnetic compound that alters the signal intensity of specific parts on MR images by shortening longitudinal relaxation time (T_1) and transverse relaxation time (T_2) of water protons in the biological tissues. The efficiency of an MRI contrast agent is quantified *in vitro* by its longitudinal and transverse relaxivities (r_1 and r_2), which reflect the ability of the contrast agent to decrease T_1 and T_2 relaxation times of the water protons, respectively. In particular, T_2-weighted contrast agents decrease MRI signal intensity and thus darken regions where they accumulate (while those where they are absent, like a liver tumour, appear brighter). The most effective T_2-weighted contrast agents are those characterized by the highest r_2/r_1 ratio. USPIOs can also be used as T_1-contrast agents, but only as long as their r_2/r_1 ratio remains at a value lower than 3, typically [49]. Relaxometry studies were performed on magnetic polymersomes loaded with two different size and loading contents of USPIOs, namely at 32% FWR with those of 4.2 nm diameter and 16 % FWR for the 7.6 nm diameter ones. Relaxation rates $1/T_1$ (s^{-1}) and $1/T_2$ (s^{-1}) were measured at 20 and 60 MHz (37°C) at different iron concentrations (mM). The plots of the relaxation rates *versus* equivalent iron concentration are given in Fig. 5. Longitudinal and transverse relaxivities deduced from the slopes are reported in Table 4. Encapsulation of USPIOs into the hydrophobic membranes of PEO_{45}-*b*-PCL_{111} polymersomes leads to a significant decrease of r_1 (due to a reduced accessibility of water protons to USPIO surface), and an increase of r_2 (due to USPIO clustering into the vesicle) compared to USPIOs individually dispersed in the solvent (see r_1 and r_2 values in THF in Table 2). In addition, it is well-known in the literature of MRI contrast agents [50] that r_1 decreases as a function of the applied magnetic field while r_2 reaches a plateau value. Consequently, higher transverse to longitudinal relaxivity ratios (r_2/r_1) were obtained at 60 MHz compared to those at 20 MHz.

DOI: 10.1039/C9TB00909D

Table 4. Longitudinal (r_1) and transverse (r_2) relaxivities (in water and at 37°C) and resulting r_2/r_1 ratios of USPIO loaded in PEO_{45}-*b*-PCL_{111} vesicle membranes.

Sample	Frequency (MHz)	r_1 ($s^{-1}\cdot mM^{-1}$)	r_2 ($s^{-1}\cdot mM^{-1}$)	r_2/r_1
PEO_{45}-*b*-PCL_{111} + 7.6 nm USPIO at 16% FWR	20	3.3	187	57
	60	1.3	197	154
PEO_{45}-*b*-PCL_{111} + 4.2 nm USPIO at 32% FWR	20	0.6	109	171
	60	0.3	110	389

As already reported in the literature for vesicles made from other copolymers, higher transverse relaxivities were obtained for polymersomes loaded with larger USPIOs [14, 46]. In this work, polymer vesicles loaded at 16% FWR with 7.6 nm USPIO have a transverse relaxivity of 197 $s^{-1}\cdot mM^{-1}$ (60 MHz) while those loaded at 32% FWR with 4.2 nm USPIO have a smaller transverse relaxivity of 110 $s^{-1}\cdot mM^{-1}$ (60 MHz). Interestingly, polymersomes loaded with 4.2 nm exhibit significantly lower longitudinal relaxivities: r_1 = 0.3 $s^{-1}\cdot mM^{-1}$ at 60 MHz compared to r_1 = 1.3 $s^{-1}\cdot mM^{-1}$ for vesicles loaded with 7.6 nm USPIOs.

This can be explained by their total embedding within the hydrophobic PCL blocks of the membranes (of thickness 21 nm according to SANS, much larger than 4.2 nm), thereby avoiding any direct contact of the water molecules with the iron oxide surface (thus preventing the contribution of the so-called "Inner Sphere" mechanism [50] to proton relaxations). Therefore even higher transverse to longitudinal relaxivity ratios (r_2/r_1) were obtained for vesicles loaded with smaller USPIOs compared to the larger ones, thereby demonstrating their high potential as T_2-contrast agents despite their lower transverse relaxivity, however that is analogous to the one of commercial SPIO MRI contrast agents.

NMRD profiles were recorded on polymersomes loaded with USPIOs possessing a diameter of 4.2 nm at 32% FWR and 7.6 nm at 16% FWR (Fig. S7 in supporting information). One can clearly note that longitudinal relaxivities of polymer vesicles loaded with the smallest USPIO (4.2 nm USPIO) are lower than those of vesicles loaded with largest USPIO (7.6 nm USPIO) over the whole range of measured frequencies. Compared to the NMRD profiles of individual USPIOs in THF (Fig. S4), a shift of the maxima towards lower Larmor frequencies were observed, and became more pronounced when the diameter of incorporated USPIOs was larger. A similar shift was already reported for PGA-*b*-PTMC vesicles incorporating USPIOs of different sizes [46] and ascribed to their embedding in the membranes, making them behave as aggregates of larger size than individually dispersed USPIOs.

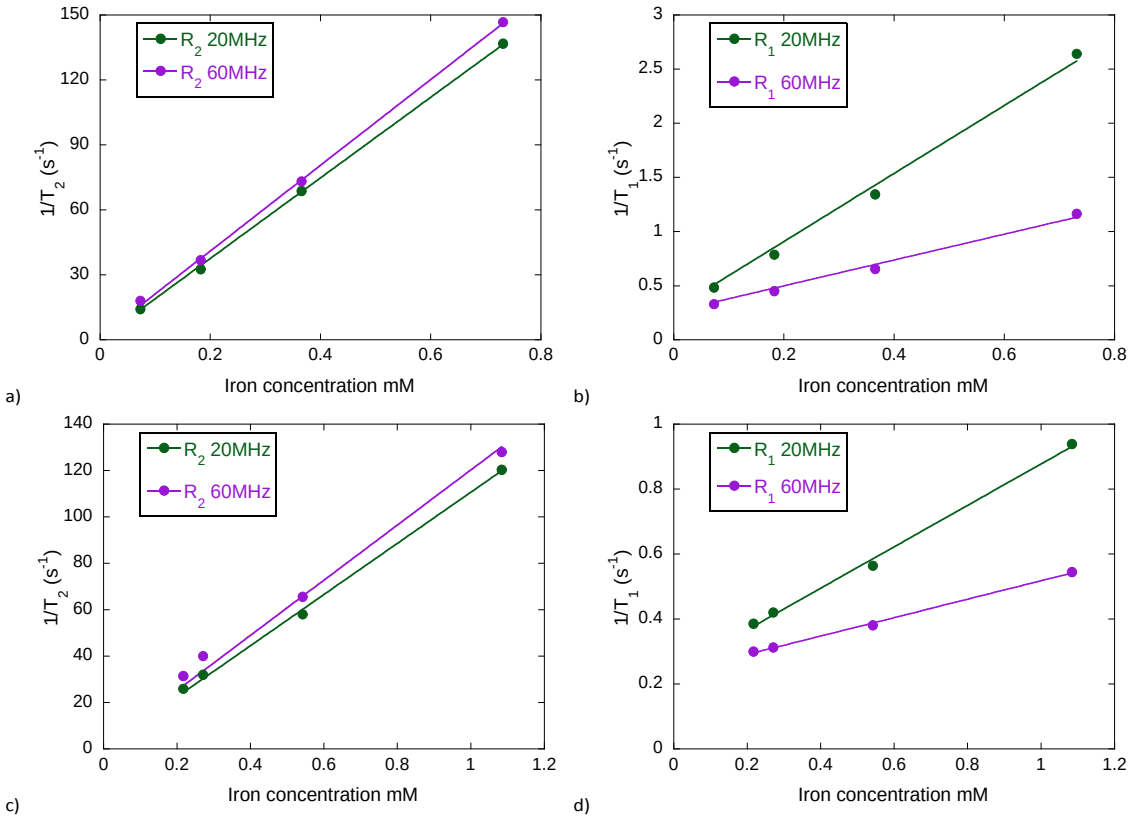

Figure 5. Relaxations rates as a function of iron concentration (mM) for PEO_{45}-*b*-PCL_{111} vesicles loaded with iron oxides nanoparticles: (a) $1/T_2$ (s^{-1}) for vesicles loaded at 16% FWR with 7.6 nm USPIOs: slopes and intercepts are r_2=186 $s^{-1}\cdot mM^{-1}$ and R_2^0=0.506 s^{-1} at 20MHz, r_2=198 $s^{-1}\cdot mM^{-1}$ and R_2^0=1.54 s^{-1} at 60MHz. (b) $1/T_1$ (s^{-1}) for vesicles loaded with 7.6 nm USPIOs at 16% FWR: slopes and intercepts are r_1=3.14 $s^{-1}\cdot mM^{-1}$ and R_1^0=0.28 s^{-1} at 20MHz, r_1=1.19 $s^{-1}\cdot mM^{-1}$ and R_1^0=0.26 s^{-1} at 60MHz. (c) $1/T_2$ (s^{-1}) for vesicles loaded with 4.2 nm USPIOs at 32% FWR: slopes and intercepts are r_2=110 $s^{-1}\cdot mM^{-1}$ and R_2^0=0.506 s^{-1} at 20MHz, r_2=119 $s^{-1}\cdot mM^{-1}$ and R_2^0=1.54 s^{-1} at 60MHz. (d) $1/T_1$ (s^{-1}) for vesicles loaded with 4.2 nm USPIOs at 32% FWR: slopes and intercepts are r_1=0.638 $s^{-1}\cdot mM^{-1}$ and R_1^0=0.24 s^{-1} at 20MHz, r_1=0.283 $s^{-1}\cdot mM^{-1}$ and R_1^0=0.235 s^{-1} at 60MHz

ARTICLE

View Article Online
DOI: 10.1039/C9TB00909D

In addition, the inflection points observed at low fields (below 1 MHz) on the NMRD profiles of individual USPIOs, usually ascribed to Néel relaxation of the moments, are absent on the NMRD profiles of the magnetic vesicles. These were fitted using the usual "Outer Sphere" model for superparamagnetic MRI contrast agents. Parameters extracted from these fittings (D^{NMRD} and M_S^{NMRD}) are reported in Table S1 (supporting information). Compared to individually dispersed USPIOs, an increase of D^{NMRD} and a decrease of M_S^{NMRD} were observed. These results are in agreement with the presence of a hydrophobic polymer layer surrounding the nanoparticles, preventing water molecules to approach surface of the magnetic centre (thus avoiding any Inner Sphere contribution to proton relaxation). The decreased magnetization values can be easily understood by the dilution of the magnetic iron oxide within the non-magnetic phase. It is also very interesting to note that the values of "Outer Sphere" diameters D^{NMRD} deduced from the fits are nearly equal to the hydrophobic membrane thickness measured by SANS (20.8 nm for 7.6 nm USPIOs at 16% FWR and 18.2 nm for 4.2 nm ones at 32% FWR). This parameter deduced by relaxometric experiments corresponds to a characteristic distance on which the presence of water molecules is forbidden, thus it is equal to the membrane hydrophobic thickness as from SANS and TEM.

In addition to their use as MRI contrast agents, magneto-vesicles described in the present study can also be used for magnetic separation, as they are retained by a LS column™ placed in an electromagnet, which confirms their high USPIO content. A study reported that magneto-liposomes containing a low amount of ferrofluid are not retained on the same magnetic column [51]. Size distributions (Fig. S8), TEM images (Fig. S9) and proton NMR relaxivities (Table S2 in supporting information) before and after magnetic chromatography are similar, which suggests that the samples are not affected by the magnetic chromatography and can therefore be concentrated by this method. Magnetophoretic separation can also be used to purify the sample and change the external aqueous medium, after loading with a hydrosoluble drug such as doxorubicin for example [52].

Degradation of USPIO loaded in PEO_{45}-*b*-PCL_{111} vesicles in acidic aqueous conditions.

The degradation of PEO_{45}-*b*-PCL_{111} based magneto-polymersomes (encapsulating 7.6 nm USPIOs at 16% FWR) was studied in weakly acidic conditions, mimicking biologically relevant conditions as tumour environment or intra-lysosomal location after cell uptake. It is indeed known that hydrolysis of polyesters shortens hydrophobic blocks and consequently increases the hydrophilic mass fraction of block copolymer chains. Such degraded chains with comparatively short hydrophobic blocks will perturb local bilayer curvature and induce the growth of pores in polymersome membranes [29, 53-55]. Poration of polyester membranes at acidic pH is particularly interesting for drug delivery purpose as it can induce drug release from polymersomes uptaken by biological cells through an endocytosis pathway that end up in acidic (pH around 5) lysosomal compartments [29, 54].

To evaluate if the overall structure is affected or not by the acidic pH, GPC, DLS and TEM measurements performed at pH 7 were compared to the results obtained at weakly acidic pH (pH 5) after 7 days. The TEM images of the sample left 7 days at pH 7 and 37°C are similar to those of the sample left at pH 5 and 37°C. Spherical nanostructures with a high USPIO content as well as some filamentous fragments were observed (Fig. S10a and Fig. S10b in supporting information). DLS measurements also show similar size distributions (sample left at pH 7 and at pH 5) with mean hydrodynamic diameters in the range between 130 and 150 nm and PDI^{DLS} values smaller than 0.17 (Fig. S10c and Fig. S10d in supporting information). This suggests that spherical structures loaded with iron oxide nanoparticles were still present in the suspensions even after one week (~168 hours) at 37°C and pH 5.

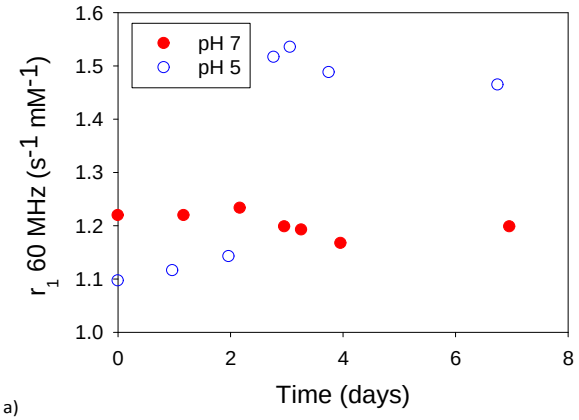

a)

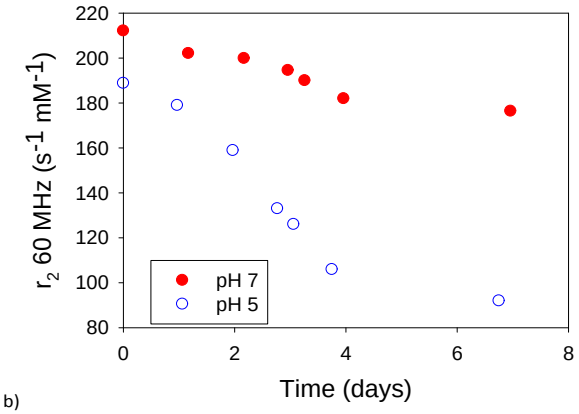

b)

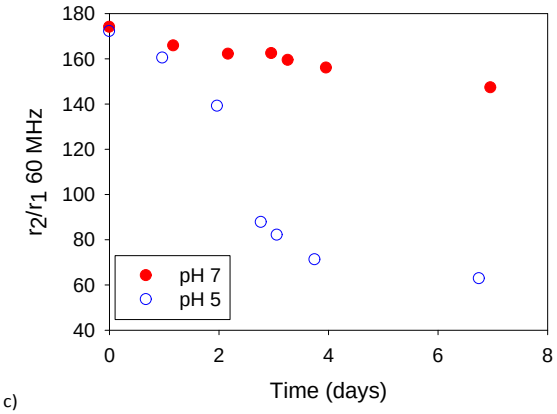

c)

DOI: 10.1039/C9TB00909D

Figure 6. Longitudinal relaxivities (a), transverse relaxivities (b) and transverse to longitudinal relaxivity ratios (c) at 60 MHz for PEO45-b-PCL111 vesicles loaded at 16% FWR with 7.6 nm USPIOs at pH 7 (red filled markers) and pH 5 (blue empty markers) as a function of time.

In parallel, the relaxivities of polymer vesicles loaded at 16% FWR with 7.6 nm USPIO were measured over time at two different pH (pH 7 and pH 5). Figure 6 shows results obtained at 60 MHz. Similar trends were observed at 20 MHz as shown in supporting information (Fig. S11). At pH 7 and at 37°C, longitudinal and transverse relaxivities did not vary significantly during the studied period (7 days). On the contrary, at pH 5, the longitudinal relaxivity increases abruptly and the transverse relaxivity decreases more continuously over time, which results in an sigmoid decrease of the transverse to longitudinal relaxivity ratio (r_2/r_1), with a jump occurring after 2 days of sample acidolysis. These relaxivity variations can be interpreted by the formation of hydrophilic pores in the PCL membranes occurring as the hydrophobic PCL block is progressively hydrolysed [25, 50, 51]. Water molecules could pass through PCL membrane leading to an increase of r_1 (due to an increased accessibility of water protons directly to the USPIO surface) and a decrease of r_2 (due to a reduced USPIO clustering effect). Such polymer degradation has been further highlighted by GPC for empty vesicles (Fig. 7), for which we could notice the appearance of a second peak at higher retention time corresponding to a M_n ~ 2600 g·mol^{-1}, and attributable to PEG chains liberated in the medium, presumably still joined to a much degraded PCL block.

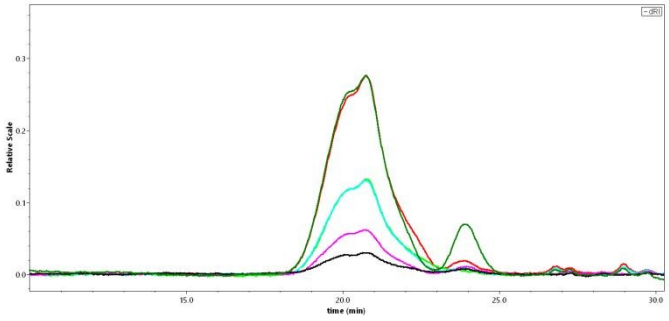

Figure 7. GPC traces in THF (RI detector) of the copolymer dissolved in two different buffers (pH7.4 and pH5.2) after dialysis, freeze-drying and recovery in THF at different times. The main peak around an elution volume of 20 mL correspond to following molar masses expressed relatively to the PS standard curve: M_n=12000 g·mol^{-1} and M_w= 15700 g·mol^{-1} at t=0;, M_n=11700 g·mol^{-1} and M_w= 15800 g·mol^{-1} at t=24h (pH5; flashy green curve); M_n=12300 g·mol^{-1} and M_w= 16200 g·mol^{-1} at t=72h (pH5; blue curve); M_n=12600 g·mol^{-1} and M_w= 16500 g·mol^{-1} at t=144h (pH5; pink curve); M_n=12400 g·mol^{-1} and M_w= 17000 g·mol^{-1} at t=168h (pH5; black curve); M_n=12800 g·mol^{-1} and M_w= 16600 g·mol^{-1} at t=208h (pH5; dark green curve); M_n=12100 g·mol^{-1} and M_w= 16000 g·mol^{-1} at t=208h (pH7). After 72h at pH5, a second peak appeared around 24 mL, corresponding to M_n=2600 g·mol^{-1} and M_w= 2700 g·mol^{-1}. This secondary peak represent 1.6% of the total weight at t=72h (assuming identical refraction index increments), increasing to 8% at t=144h until reaching a plateau at 11% for t=168h. This peak is also present, yet at lower extent (3% of total weight) after 208h at pH7 (red curve), and can be ascribed to PEG 2kD chains linked to a much degraded PCL block.

This peak appeared 72 hours (3 days) after incubation at pH5.2, and was also observable, at lower extent, after 208 hours at pH7.4. This result confirms the slow acidolysis of the PCL blocks. Although the vesicles did not show any sign of disruption neither by TEM nor DLS, their relaxometric data proved access of the water molecules to the USPIO surfaces, thus enhanced permeability of the membranes after only 2 days at pH5. This MRI response is even more sensitive than by measuring molecular dimension of the chains by GPC, which showed clear evidence of chain cleavage, but only after 3 days at pH5.2.

In future *in vivo* experiments, such variations of r_1 and r_2 could be turned into a greater advantage to monitor experimentally the PCL degradation in the membrane drug-nanocarriers from the modulation of the contrast of MR images and correlate the evidenced drug release with anatomic information (*e.g.* tumour volume). An enhanced MRI contrast following a controlled drug release and accumulation to diseased organs/tissues is very promising for *in vivo* applications [56, 57].

In previous literature, D. Hammer *et al.* showed that hydrolytic degradation of PEO-*b*-PCL vesicles incorporating porphyrin-based fluorophores within the PCL core results in change in porphyrin emission providing a powerful tool for monitoring in vivo drug delivery non-invasively [34]. Such degradative mechanism of polyester-made vesicles, catalysed by enzymes, was also reported in recent work by Zhu *et al.* [58]. However, to the authors' knowledge, no similar work using MRI contrast agents to monitor degradation of polyesters like PCL in membranes was never reported. The novelty of our work stands in the proof that this phenomenon strongly influences the MRI contrasting properties. To show the interest of PEO_{45}-*b*-PCL_{111} vesicles loaded with USPIOs for monitoring degradation of PCL membrane of nanovesicles *in vivo*, we computed the signal levels by the approximated solution of Bloch equations, a method that we used in a precedent study [49] to predict the evolution of MR image contrast from proton NMR relaxometric measurements:

$$S_{MRI} \propto \rho_H \left(1 - e^{-TR/T_1}\right) \cdot e^{-TE/T_2} \qquad (3)$$

Where S_{MRI} corresponds to the theoretical MRI signal intensity, ρ_H corresponds to the proton volume density, TR is the repetition time and TE is the echo time.

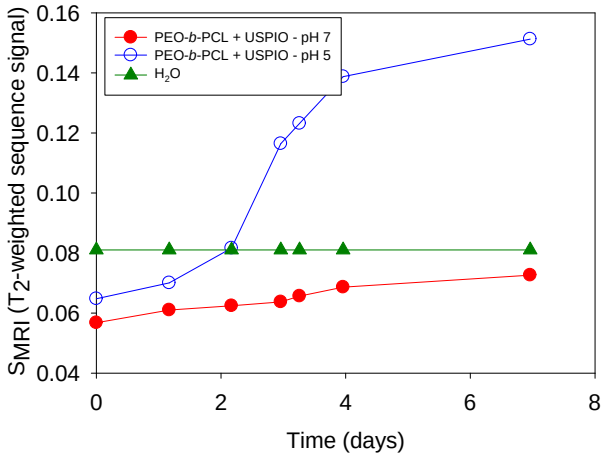

Figure 8. Theoretical predictions of MRI signal levels computed using Eqn (3) with the experimental values of T_1, T_2, TE and TR for water (green triangular filled markers) and PEO_{45}-*b*-PCL_{111} vesicles loaded at 16% FWR with 7.6 nm USPIO at pH 7 (red circular filled markers) and pH 5 (blue circular empty markers) as a function of time.

ARTICLE DOI: 10.1039/C9TB00909D

The S_{MRI} calculated with experimental T_1 and T_2 are represented for a T_2-weighted sequence (TR = 300 ms, TE = 12 ms) on Fig. 8, and their numerical values are provided on Table 5. At pH 7, S_{MRI} does not change significantly with time. On the contrary, S_{MRI} increases with time at pH 5 due to hydrolytic degradation of PCL membrane resulting in an increase of r_1 and a decrease of r_2. Again, the interest of these magnetic nano-vesicles made of a hydrolysable copolymer is evidenced, by the predicted positive contrast enhancement of MRI signal.

Table 5. Longitudinal (T_1) and transverse (T_2) proton relaxation times for PEO_{45}-*b*-PCL_{111} vesicles loaded with 16 wt.% 7.6 nm USPIOs measured at 60 MHz (37°C) at pH 5 and pH 7 and resulting SMRI calculated from Eqn (3) for a T_2-weighted sequence (TR = 300 ms, TE = 12 ms).

	pH 7			pH 5		
Time (hours)	T_1 (ms)	T_2 (ms)	S_{MRI}	T_1 (ms)	T_2 (ms)	S_{MRI}
0	986	7.84	0.057	1093	9.16	0.065
28	986	8.23	0.061	1080	9.66	0.070
52	978	8.32	0.062	1062	10.88	0.081
71	998.5	8.55	0.064	864	12.98	0.116
78	1002	8.75	0.066	856	13.70	0.123
95	1017.5	9.14	0.069	877	16.29	0.139
167	998.5	9.42	0.073	887	18.74	0.151

Conclusions

Iron oxide nanoparticles possessing two different sizes (D^{TEM} = 4.2±0.5 nm and D^{TEM} = 7.6±1.6 nm) were produced by the thermal decomposition method of iron(acac)$_3$ precursor. These hydrophobically-coated USPIO nanoparticles were easily incorporated into PEO_{45}-*b*-PCL_{111} vesicles by a nanoprecipitation method at maximal feed weight ratios (FWR) of 32% and 16%, respectively. Extrusion cycles were performed to produce vesicles around 150 – 180 nm in diameter with a narrow size distribution, ideal for *in vivo* applications, including systemic injection. In addition to their biocompatible and biodegradable composition, vesicles possess PEO chains on their surface which are known to confer "stealth" properties to the nanoparticles *in vivo*, *i.e.* a prolonged half-life (long $T_{1/2}$) in the blood circulation that is a prerequisite for an efficient drug delivery system.

Magnetic polymeric vesicles with high USPIO contents were obtained by optimizing the initial FWR. These magneto-polymersomes show good MRI contrasting properties at 20 and at 60 MHz, the second resonance frequency being close to the one in the field of most MRI scanners used in clinics. They are characterized by very high transverse-to-longitudinal relaxivity ratios (r_2/r_1), which demonstrates that they are very promising candidates as T_2-contrast agents for at least pre-clinical studies. Relaxivities of polymer vesicles embedded with USPIO possessing two different sizes were compared. Results confirmed that magneto-polymersomes incorporating larger USPIOs possess higher transverse relaxivity (yet at a lower FWR). We showed that the size of the embedded USPIOs plays also a critical role on the longitudinal relaxivity: PEO_{45}-*b*-PCL_{111} polymersomes loaded at 32% FWR with 4.2 nm USPIO possess significantly lower longitudinal relaxivities and higher r_2 to r_1 ratios than vesicles loaded with 7.6 nm USPIOs at 16% FWR, which was interpreted by the total embedding of the USPIOs within the membranes (none of them being located near the hydrated PEG blocks of the copolymer).

Relaxometry studies at pH 5 *vs* pH 7, combined with a complementary test of copolymer chain degradation by GPC, confirm the formation of pores in PCL membrane in acidic conditions. These findings demonstrate the huge potential of the magneto-polymersomes described in the present study as drug delivery systems with image-control by MRI of the sustained release of encapsulated therapeutics in weakly acidic media such as tumours and intracellular endo/lysosomal compartments. Variations of r_1 and r_2 relaxivities along the PCL hydrolysis illustrate that these superparamagnetic PEO_{45}-*b*-PCL_{111} vesicles are promising pH-sensitive MRI contrast agents enabling to track the PCL chain degradation accompanying the delivery of pre-encapsulated species *in vivo*.

Conflicts of interest

There are no conflicts to declare.

Acknowledgements

The authors thank the department of histology (Prof. D. Nonclercq) of the University of Mons and X. Valentini for providing the access to TEM apparatus. Dr. L. Mespouille (SMPC; UMons) and Dr. J de Winter (S2Mos; UMons) are warmly acknowledged for providing the polymers used during this study. The authors are grateful to Prof. O. Ersen and D. Ihiawakrim from "Institut de Physique et Chimie des Matériaux de Strasbourg (IPCMS)" from the University of Strasbourg from cryo-TEM analysis and Amélie Vax-Weber and C. Pierart for performing respectively the GPC and ICP measurements. The authors acknowledge the Center for Microscopy and Molecular Imaging (CMMI). This work was performed with the financial support of the FNRS, the Agence Nationale de la Recherche (ANR-13-BS08-0017 MagnetoChemoBlast), the ARC program, the ENCITE program and the RW, the Interuniversity Attraction Poles of the Belgian Federal Science Policy Office, and the European Commission under COST (European Cooperation in Science and Technology) Action TD1402 RadioMag. The financial support from the CPER CAMPUSB project funded by the French state and the Région Nouvelle Aquitaine is gratefully acknowledged for the acquisition of the multi-angle light-scattering setup.

Notes and references

1 C. Geraldes and S. Laurent, *Contrast Media & Molecular Imaging*, 2009, **4**, 1.
2 Y. Gossuin, P. Gillis, A. Hocq, Q. L. Vuong and A. Roch, *Wiley Interdisciplinary Reviews: Nanomedicine and Nanobiotechnology*, 2009, **1**, 299.
3 Q. A. Pankhurst, J. Connolly, S. K. Jones and J. Dobson, *Journal of Physics D: Applied Physics*, 2003, **36**, R167.
4 S. Laurent, D. Forge, M. Port, A. Roch, C. Robic, L. Vander Elst and R. N. Muller, *Chemical Reviews*, 2008, **108**, 2064.
5 S. Laurent, J. Bridot, L. Vander Elst and R. N. Muller, *Future Medicinal Chemistry*, 2010, **2**, 427.
6 S. Belaïd, S. Laurent, M. Vermeersch, L. Vander Elst, D. Perez-Morga and R. N. Muller, Nanotechnology, 2013, **24**, 055705.

DOI: 10.1039/C9TB00909D

7 D. Stanicki, L. Vander Elst, R. N. Muller and S. Laurent, *Current Opinion in Chemical Engineering*, 2015, **8**, 7.
8 N. A. Frey, S. Peng, K. Cheng and S. Sun, *Chemical Society Reviews*, 2009. **38,** 2532.
9 D. Ling and T. Hyeon, *Small*, 2013, **9**, 1449.
10 E. Peng, F. Wang and J.M. Xue, *Journal of Materials Chemistry B*, 2015, **3**, 2241.
11 H. Ai, C. Flask, B. Weinberg, X. T. Shuai, M. D Pagel, D. Farrell, J. Duerk, and J. Gao, *Advanced Materials*, 2005, **17**, 1949.
12 H. GB, R. Zhou Jx Fau - Yuan and Y. RX, *Int J Nanomedicine*, 2012, **7**, 2863.
13 R. J. Hickey, A. S. Haynes, J. M. Kikkawa and S.-J. Park, *Journal of the American Chemical Society*, 2011, **133**, 1517.
14 R. J. Hickey, J. Koski, X. Meng, R. A. Riggleman, P. Zhang and S.-J.Park, *ACS Nano*, 2014, **8**, 495.
15 R. Bleul, R. Thiermann, G. U. Marten, M. J. House, T. G. St Pierre, U. O. Hafeli and M. Maskos, Nanoscale, 2013, **5**, 11385.
16 C. Sanson, O. Diou, J. Thévenot, E. Ibarboure, A. Soum, A. Brûlet, S. Miraux, E. Thiaudière, S. Tan, A. Brisson, V. Dupuis, O. Sandre and S. Lecommandoux, *ACS Nano*, 2011, **5**, 1122.
17 S. Lecommandoux, O. Sandre, F. Chécot, J. Rodriguez-Hernandez, and R. Perzynski, *Advanced Materials*, 2005, **17**, 712.
18 J. Du and R.K. O'Reilly, *Soft Matter*, 2009, **5**, 3544.
19 J. JP, N. Ayen Wy Fau - Kumar, and K. N, *Curr Pharm Des*, 2011, **17**, 65.
20 F. Meng, Z. Zhong and J. Feijen, *Biomacromolecules*, 2009, 10, 197.
21 F. Ahmed, R. I. Pakunlu, A. Brannan, F. Bates, T. Minko and D. E. Discher, *Journal of Controlled Release*, 2006, **116**, 150.
22 H. De Oliveira, J. Thevenot and S. Lecommandoux, *Wiley Interdisciplinary Reviews: Nanomedicine and Nanobiotechnology*, 2012, **4**, 525.
23 M-T. Popescu and C. Tsitsilianis, *ACS Macro Letters*, 2013, **3**, 222.
24 J. Qin, Q. Liu, J. Zhang, J. Chen, S. Chen, Y. Zhao, J. Du, *ACS Appl Mater Interfaces*, 2015, **7(25)**, 14043.
25 T. Ren, Q. Liu, H. Lu, X. Zhang, J. Du, *J. Mater. Chem*., 2012, **22**, 12329.
26 Q. Liu, L. Song, S. Chen, J. Gao, P. Zhao, J. Du, *Biomaterials*, 2017, **114**, 23.
27 J.-F. Le Meins, O. Sandre and S. Lecommandoux, *The European Physical Journal E*, 2011, **34**, 14.
28 M. Krack, H. Hohenberg, A. Kornowski, P. Lindner, H. Weller, and S. Förster, *Journal of the American Chemical Society*, 2008, **130**, 7315.
29 P. P. Ghoroghchian, G. Li, D. H. Levine, K. P. Davis, F. S. Bates, D. A. Hammer and M. J. Therien, *Macromolecules*, 2006, **39**, 1673.
30 D. J. Adams, C. Kitchen, S. Adams, S. Furzeland, D. Atkins, P. Schuetz, C. M. Fernyhough, N. Tzokova, A. J. Ryan and M. F. Butler, *Soft Matter*, 2009, **5**, 3086.
31 Z. Pang, H. Gao, Y. Yu, J. Chen, L. Guo, J. Ren, Z. Wen, J. Su and X. Jiang, *International Journal of Pharmaceutics*, 2011, **415**, 284.
32 W. Qi, P. P. Ghoroghchian, G. Li, D. A. Hammer and M. J. Therien, *Nanoscale*, 2013, **5**, 10908.
33 Z. Pang, H. Gao, J. Chen, S. Shen, B. Zhang, J. Ren, L. Guo, Y. Qian, X. Jiang and H. Mei, *International Journal of Nanomedicine*, 2012, **7**, 3421.
34 N. P. Kamat, Z. Liao, L. E. Moses, J. Rawson, M. J. Therien, I. J. Dmochowski and D. A. Hammer. *Proceedings of the National Academy of Sciences*, 2011, **108**, 13984.
35 N. Sood, W. T. Jenkins, X. -Y. Yang, N. N. Shah, J. S. Katz, C. J. Koch, P. R. Frail, M. J. Therien, D. A. Hammer and S. M. Evans *Journal of Pharmaceutics*, 2013, **2013**, 10.
36 R. Šachl, M. Uchman, P. Matějíček, K. Procházka, M. Štěpánek, and M. Špírková, *Langmuir*, 2007, **23**, 3395.
37 E. Konishcheva, D. Häussinger, S. Lörcher and W. Meier, *European Polymer Journal*, 2016, **83**, 300.
38 S. Hocine, D. Cui, M.-N. Rager, A. Di Cicco, J.-M. Liu, J. Wdzieczak-Bakala, A. Brûlet and M.-H. Li, *Langmuir*, 2013, **29**, 1356.
39 P. J. Photos, L. Bacakova, B. Discher, F. S. Bates and D. E. Discher, *Journal of Controlled Release*, 2003, **90**, 323.
40 B. G. G. Lohmeijer, R. C. Pratt, F. Leibfarth, J. W. Logan, D. A. Long, A. P. Dove, F. Nederberg, J. Choi, C. Wade, R. M. Waymouth and J. L. Hedrick, *Macromolecules*, 2006, **39**, 8574.
41 S. Abbad, C. Wang, A. Yahia Waddad, H. Lv and J. Zhou, *International Journal of Nanomedicine*, 2015, **10**, 305.
42 S. W. Provencher, *The Journal of Chemical Physics*, 1976, **64**, 2772.
43 A. Brulet, D. Lairez, A. Lapp and J.-P. *Cotton Journal of Applied Crystallography*, 2007, **40**, 165.
44 A. Roch, R.N. Muller and P. Gillis, *The Journal of Chemical Physics*, 1999, **110**, 5403.
45 F. Chécot, A. Brûlet, J. Oberdisse, Y. Gnanou, O. Mondain-Monval and S. Lecommandoux, *Langmuir*, 2005, **21**, 4308.
46 P. Arosio, J. Thevenot, T. Orlando, F. Orsini, M. Corti, M. Mariani, L. Bordonali, C. Innocenti, C. Sangregorio, H. Oliveira, S. Lecommandoux, A. Lascialfari and Olivier Sandre, *Journal of Materials Chemistry B*, 2013, **1**, 5317.
47 C. Sanson, C. Schatz, J.-F. Le Meins, A. Brûlet, A. Soum and S. Lecommandoux, *Langmuir*, 2010, **26**, 2751.
48 D. Kunz, A. Thurn and W. Burchard, *Colloid and Polymer Science*, 1983, **261**, 635.
49 A. Hannecart, D. Stanicki, L. Vander Elst, R. N. Muller, S. Lecommandoux, J. Thevenot, C. Bonduelle, A. Trotier, P. Massot, S. Miraux, O. Sandre and S. Laurent, *Nanoscale*, 2015, **7**, 3754.
50 S. Laurent, L. Vander Elst and R.N. Muller, in *Encyclopedia of Magnetic Resonance*, ed. R. K. Harris and R. Wasylishen, John Wiley, Chichester, 2009.
51 B. Garnier, S. Tan, S. Miraux, E. Bled and A. R. Brisson. *Contrast Media & Molecular Imaging*, 2012, **7**, 231.
52 P. Pradhan, J. Giri, F. Rieken, C. Koch, O. Mykhaylyk, M. Döblinger, R. Banerjee, D. Bahadur and C. Plank, *Journal of Controlled Release*, 2010, **142**, 108.
53 G.-Y. Liu, C.-J. Chen and J. Ji, *Soft Matter*, 2012, **8**, 8811.
54 F. Ahmed, R. I. Pakunlu, G. Srinivas, A. Brannan, F. Bates, M. L. Klein, T. Minko and D. E. Discher. *Molecular Pharmaceutics*, 2006, **3**, 340.
55 F. Ahmed and D.E. Discher, *Journal of Controlled Release*, 2004, **96**, 37.
56 K. Zhu, Z. Deng, G. Liu, J. Hu and S. Liu, *Macromolecules*, 2017. **50**, 1113.
57 K. Yang, Y. Liu, Y. Liu, Q. Zhang, C. Kong, C. Yi, Z. Zhou, Z. Wang, G. Zhang, Y. Zhang, N. M. Khashab, X. Chen and Z. Nie, *Journal of the American Chemical Society*, 2018, **140**, 4666.
58 Y. Zhu, A. Poma, L. Rizzello, V. M. Gouveia, L. Ruiz-Perez, G. Battaglia, C. K. WilliamsAngew. *Chem. Int. Ed*. 2019, **58**, 4581

Electronic Supplementary Material (ESI) for Journal of Materials Chemistry B.
This version is the manuscript accepted for publication DOI: 10.1039/C9TB00909D

Supporting Information

Embedding of superparamagnetic iron oxide nanoparticles into membranes of well-defined poly(ethylene oxide)-*block*-poly(ε-caprolactone) nanovesicles as ultrasensitive MRI probes of membrane bio-degradation

Adeline Hannecart,[a] Dimitri Stanicki,[a] Luce Vander Elst,[a] Robert N. Muller,[a,b] Annie Brûlet[c], Olivier Sandre,[d] Christophe Schatz,[d] Sébastien Lecommandoux[d] and Sophie Laurent*[a,b]

[a]*Department of General, Organic and Biomedical Chemistry, NMR and Molecular Imaging Laboratory, University of Mons, 19 avenue Maistriau B-7000 Mons, Belgium*

[b]*Center for Microscopy and Molecular Imaging, 8 rue Adrienne Bolland, B-6041 Charleroi, Belgium*

[c]*Laboratoire Léon Brillouin, UMR12 CNRS / CEA Saclay, 91191 Gif sur Yvette, France*

[d]*Laboratoire de Chimie des Polymères Organiques, UMR5629 CNRS / Université de Bordeaux, ENSCBP 16 avenue Pey Berland F-33607 Pessac, France*

Determination of the composition of PEO-*b*-PCL copolymer by ^{1}H NMR

^{1}H NMR spectrum of PEO-*b*-PCL copolymer was recorded at 500 MHz in $CDCl_3$ (Fig. S1).

The peak at 3.65 ppm is attributed to the methylene protons of the ethylene oxide units of PEO (protons B + B'). The peak corresponding to two protons of the last EO unit connected to PCL block (protons C) is lost in the background noise. As the average number of EO units is 45 (the synthesis was performed with PEO possessing an average molecular weight of 2000 g/mol), the integral intensity of the signal at 3.65 ppm (protons B and B') was set to 178.

Methylene protons of the **ε**-caprolactone units of PCL segment appeared as four signals at 4.07 ppm, 2.32 ppm, 1.65 ppm and 1.40 ppm as marked in figure S1. A degree of polymerization of PCL block (DP_{CL}) equal to 111 was determined from the integral intensity of the well-resolved peak at 4.07 ppm ($I_{4.07\ ppm}$) according to the equation S.1. The peak corresponding to two protons of the last CL unit connected to the hydroxyl group (protons H) is lost in the background noise.

$$DP_{CL} = (I_{4.07\ ppm} + 2) / 2 \qquad (S.1)$$

a)

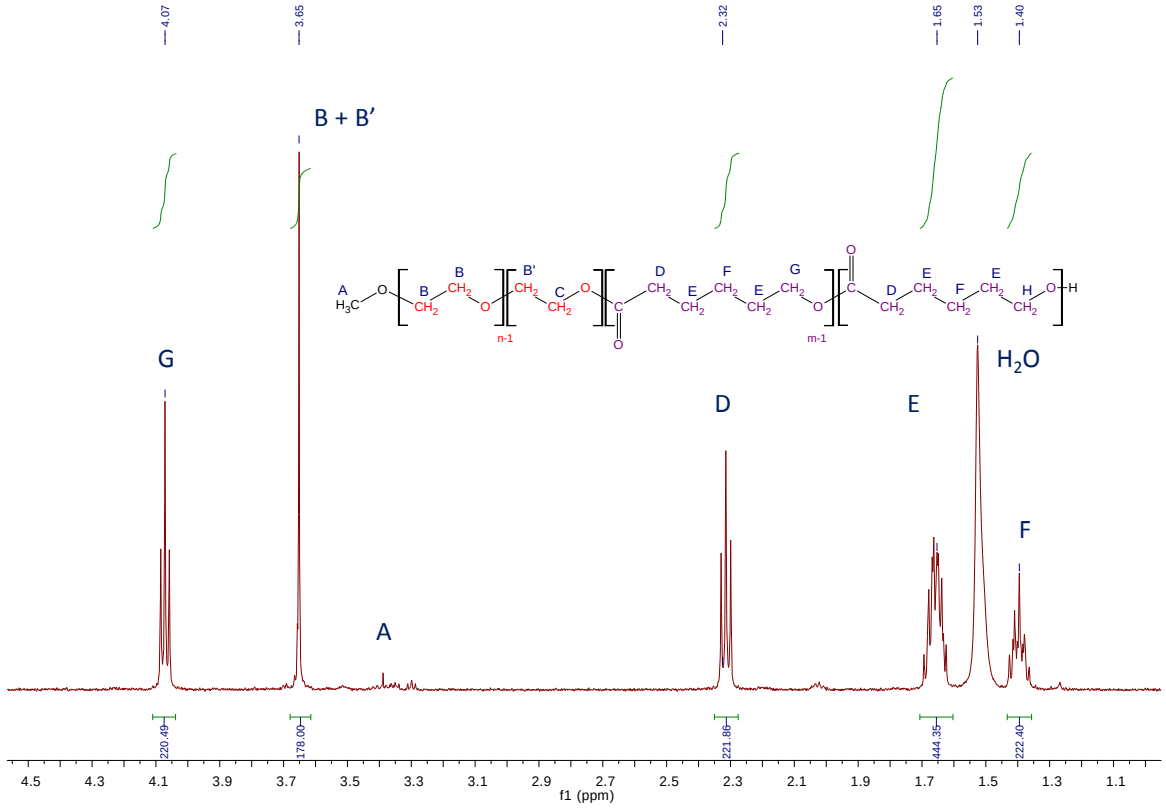

b)

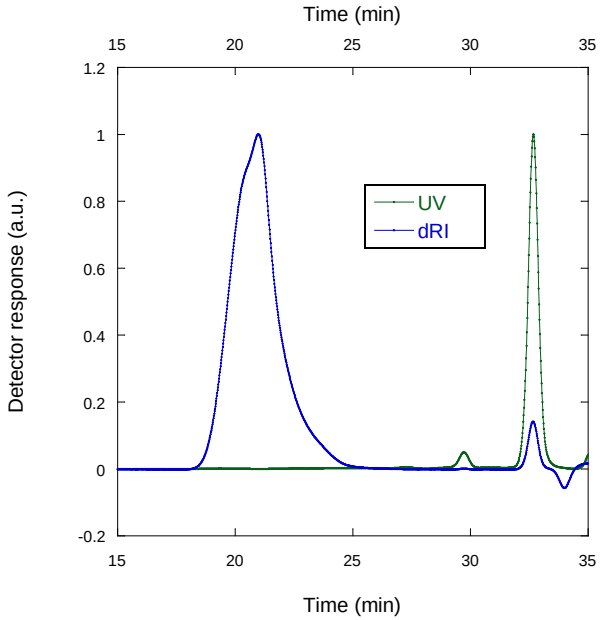

Figure S1. (a) 500 MHz ^{1}H NMR spectrum of PEO_{45}-*b*-PCL_{111} copolymer in $CDCl_3$; (b) GPC chromatogram of PEO_{45}-*b*-PCL_{111} obtained in THF (only UV and RI detector signals are plotted, the flow marker peak at 32.6 min being ascribed to 1,2,4-trichlorobenzene added in the eluent). The copolymer molar mass dispersity deduced is $Đ=M_w/M_n=1.35$.

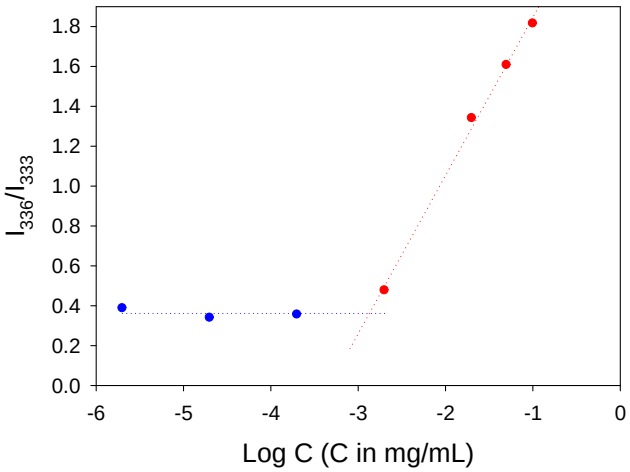

Figure S2. Plot of the I_{336}/I_{331} ratio against the logarithm of concentration of PEO_{45}-*b*-PCL_{111} suspensions in the presence of pyrene at fixed concentration of 0.6 µM.

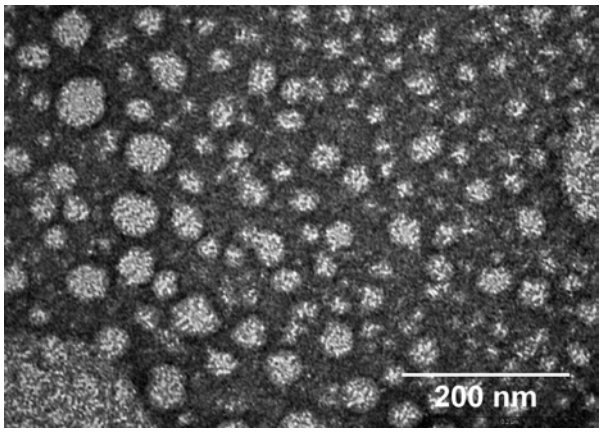

Figure S3. TEM images of PEO_{45}-*b*–PCL_{111} polymersomes negatively stained with uranyl acetate (scale bar = 200 nm)

a) b)

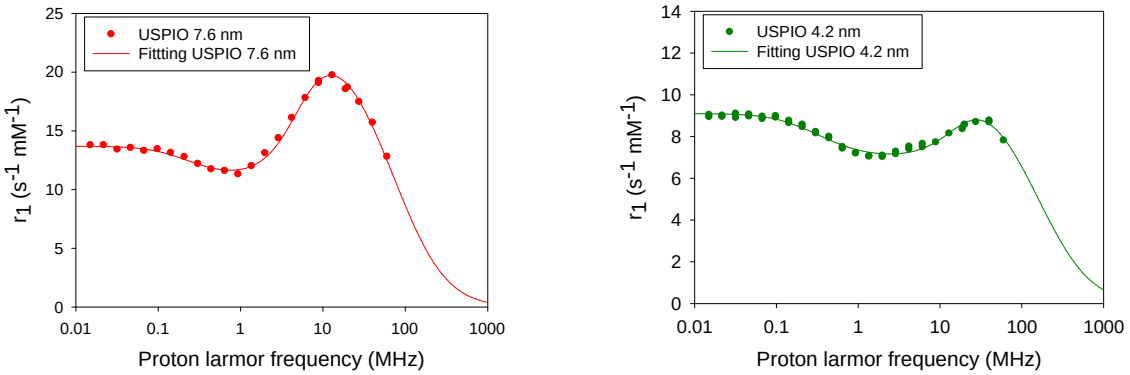

Figure S4. NMRD profiles of the longitudinal relaxivity *vs.* proton Larmor resonance frequency at 37°C for (a) 7.6 nm and (b) 4.2 nm USPIOs in THF. The fitting parameters are given in Table 1.

a) b)

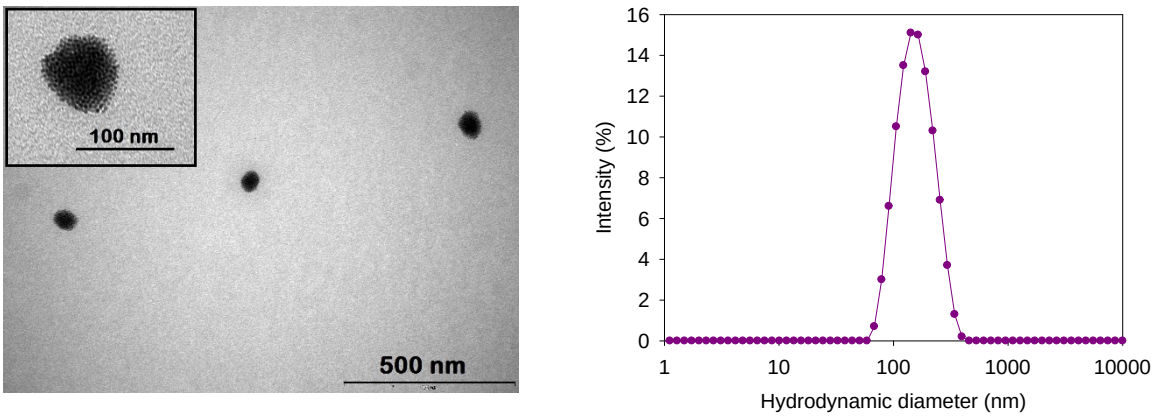

Figure S5. Size and morphology of PEO_{45}-*b*-PCL_{111} vesicles loaded at 32% FWR with iron oxide nanoparticles of 4.2 nm diameter. (a) Low magnification TEM image showing vesicles with a high payload of USPIO (scale bar = 500 nm). The inset shows a close-up view of one vesicle (scale bar = 100 nm). (b) Intensity-weighted size distribution measured by DLS (D_H = 146 nm, PDI^{DLS} = 0.10).

a) b)

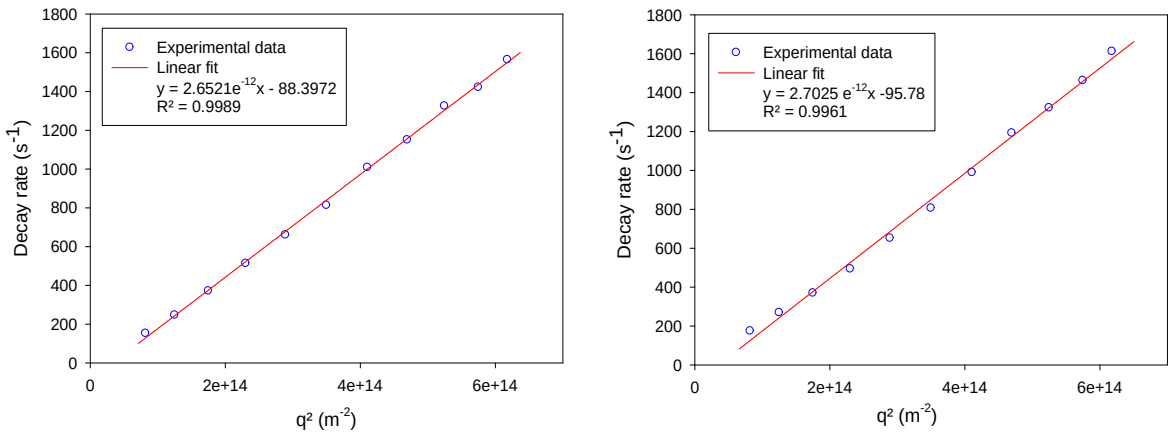

Figure S6. Multi-angle DLS plots: Variations of decay rate Γ *versus* squared scattering vector q^2 measured by multi-angle DLS by applying a CONTIN fit on a) Nanoprecipitated objects made by co-assembly of PEO_{45}-*b*-PCL_{111} with 7.6 nm USPIO at 16% FWR and at a concentration of 0.11 mg·mL^{-1}

and b) Nanoprecipitated objects by co-assembly of PEO_{45}-*b*-PCL_{111} with 4.2 nm USPIO at 32% FWR and at a concentration of 0.052 mg·mL^{-1}. The slopes lead to the diffusion constants of the objects, respectively 2.65 10^{-12} m²/s^{-1} (a) and 2.70 10^{-12} m²/s^{-1} (b), from which the hydrodynamic radii are calculated using Stokes-Einstein's equation, respectively 92.0 nm (a) and 90.3 nm (b).

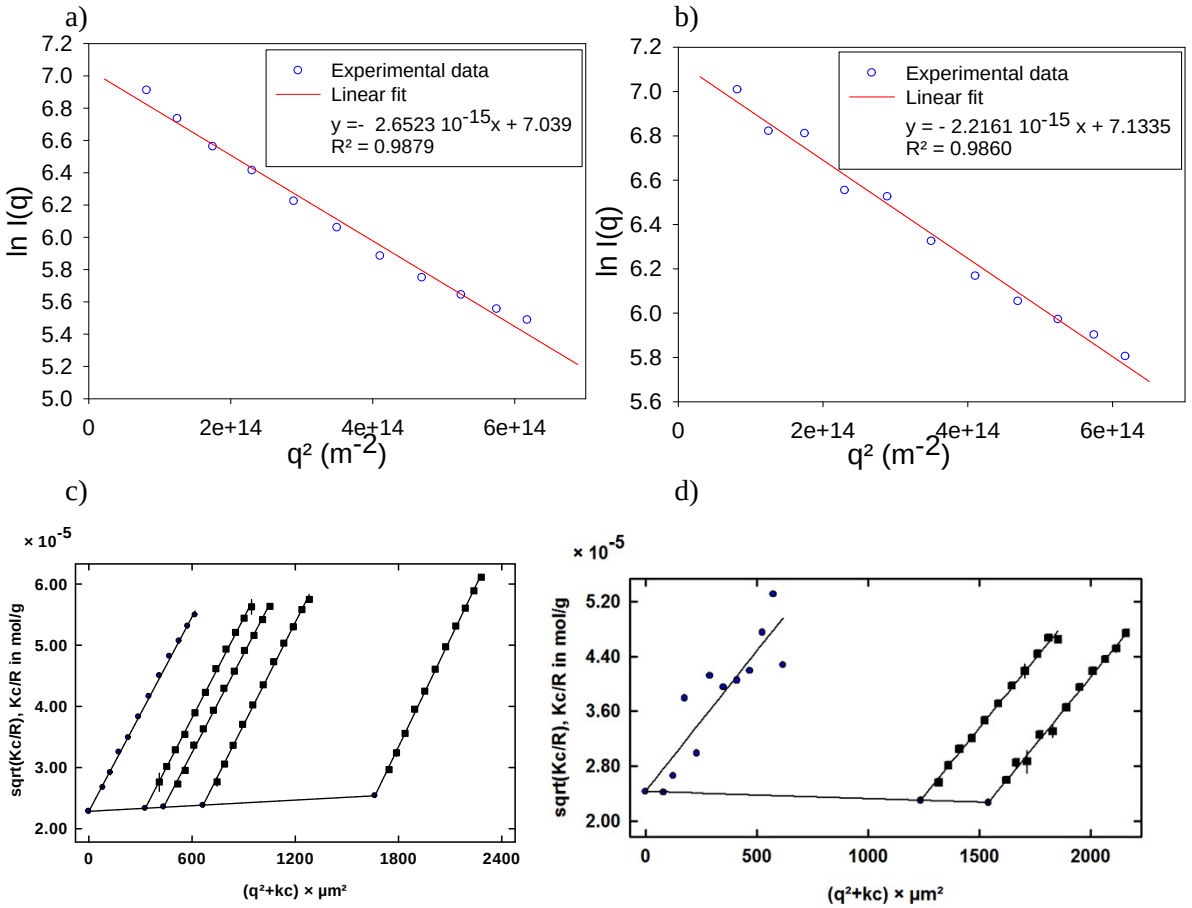

Figure S7. Multi-angle SLS plots: Guinier (a,b) and Berry (c,d) plots on nanoprecipitated objects made by co-assembly of PEO_{45}-*b*-PCL_{111} with 7.6 nm USPIOs at 16% FWR (a,c) or with 4.2 nm USPIOs at 32% FWR (b,d). Scattering angles were varied from 40° to 140° and concentrations from 0.041mg·mL^{-1} (for 4.2 nm USPIO sample) to 0.554 mg·mL^{-1} (for 7.6 nm USPIO sample).

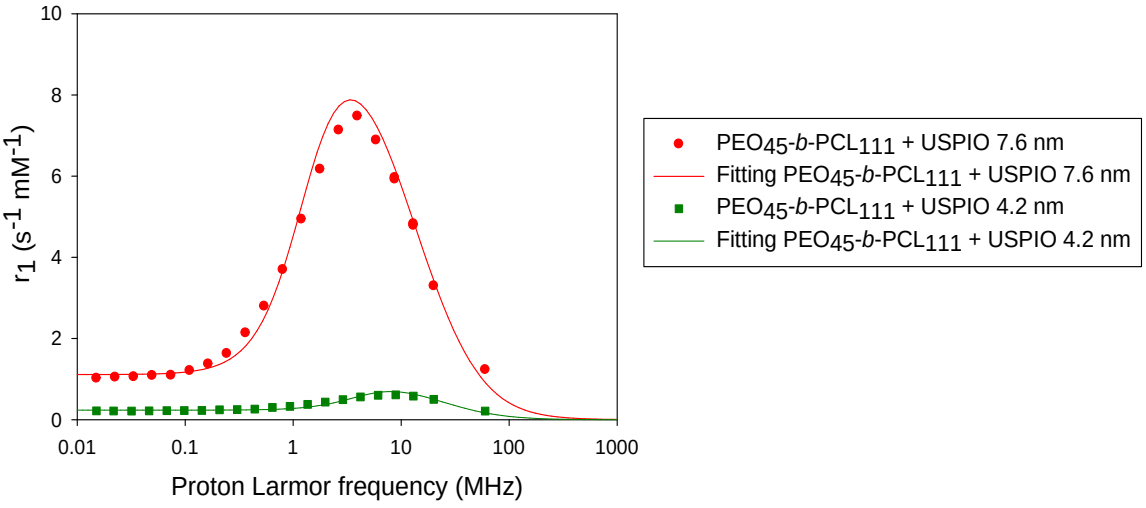

Figure S8. NMRD profiles of the longitudinal relaxivity *vs.* proton Larmor resonance frequency at 37°C for PEO_{45}-b-PCL_{111} vesicles loaded at 16% FWR with 7.6 nm USPIOs (circles) and at 32% FWR of 4.2 nm USPIOs (squares). The solid lines correspond to the MC simulation based on the theoretical model for superparamagnetic contrast agents.

Table S1. Parameters extracted from the fitted NMRD profiles (D^{NMRD} and M_S^{NMRD}) of USPIOs loaded in PEO_{45}-*b*-PCL_{111} vesicles (in water) and individually dispersed USPIOs (in THF).

Sample	D^{NMRD} (nm)	M_S^{NMRD} ($A \cdot m^2 \cdot kg^{-1}$)
PEO_{45}-*b* -PCL_{111} vesicles + 7.6 nm USPIOs at 16% FWR (in water)	20.8	14.0
7.6 nm USPIO (in THF)	8.5	49.4
PEO_{45}-*b* -PCL_{111} vesicles + 4.2 nm USPIOs at 32% FWR (in water)	18.2	5.6
4.2 nm USPIO (in THF)	5.6	49.7

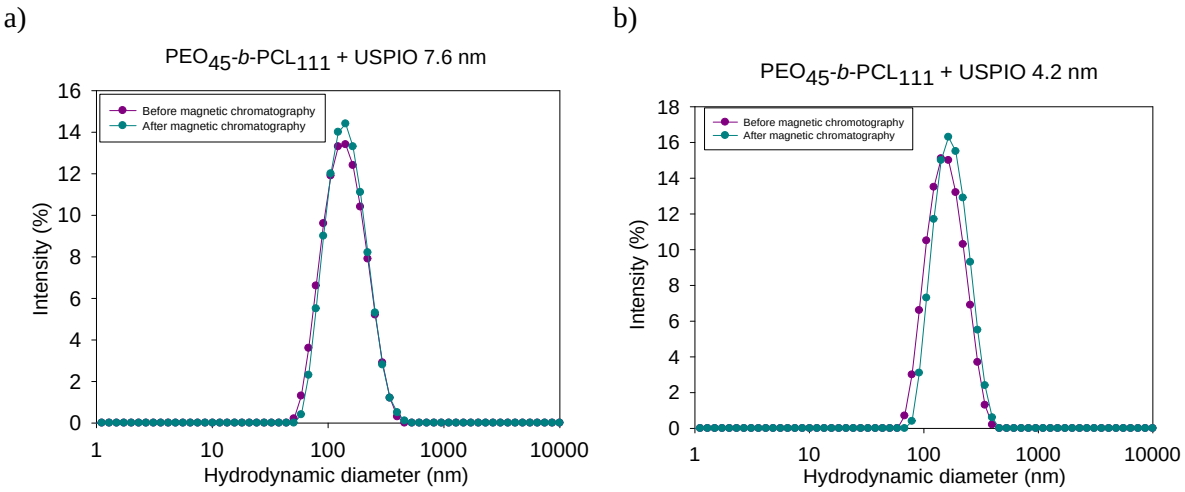

Figure S9. Intensity-weighted size distribution measured by DLS of PEO_{45}-*b*-PCL_{111} vesicles measured after synthesis and after magnetic chromatography (a) vesicles loaded at 16% FWR with USPIOs of 7.6 nm diameter and (b) vesicles loaded at 32% FWR with USPIOs of 4.2 nm diameter.

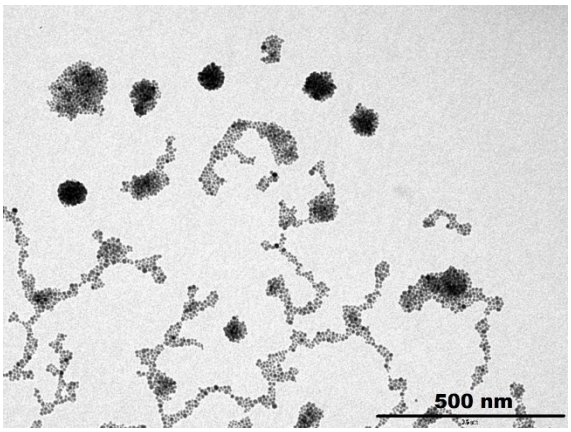

Figure S10. TEM image of PEO_{45}-*b*-PCL_{111} vesicles loaded at 16% FWR with iron oxide nanoparticles of 7.6 nm diameter after magnetic chromatography.

Table S2. Longitudinal (r_1) and transverse (r_2) relaxivities (in water and at 37°C) and resultant r_2/r_1 ratios of USPIO loaded in PEO_{45}-*b*-PCL_{111} vesicles before and after magnetic chromatography

Sample	Larmor frequency (MHz)	Before magnetic chromatography			After magnetic chromatography		
		r_1 ($s^{-1}\cdot mM^{-1}$)	r_2 ($s^{-1}\cdot mM^{-1}$)	r_2/r_1	r_1 ($s^{-1}\cdot mM^{-1}$)	r_2 ($s^{-1}\cdot mM^{-1}$)	r_2/r_1
PEO_{45}-*b*-PCL_{111} + USPIO 7.6 nm (FWR=16%)	20	3.23	187	58	2.85	172	60
	60	1.22	198	162	1.09	188	173
PEO_{45}-*b*-PCL_{111}+ USPIO 4.2 nm (FWR=32%)	20	0.64	109	171	0.55	94	171
	60	0.28	110	389	0.23	87	371

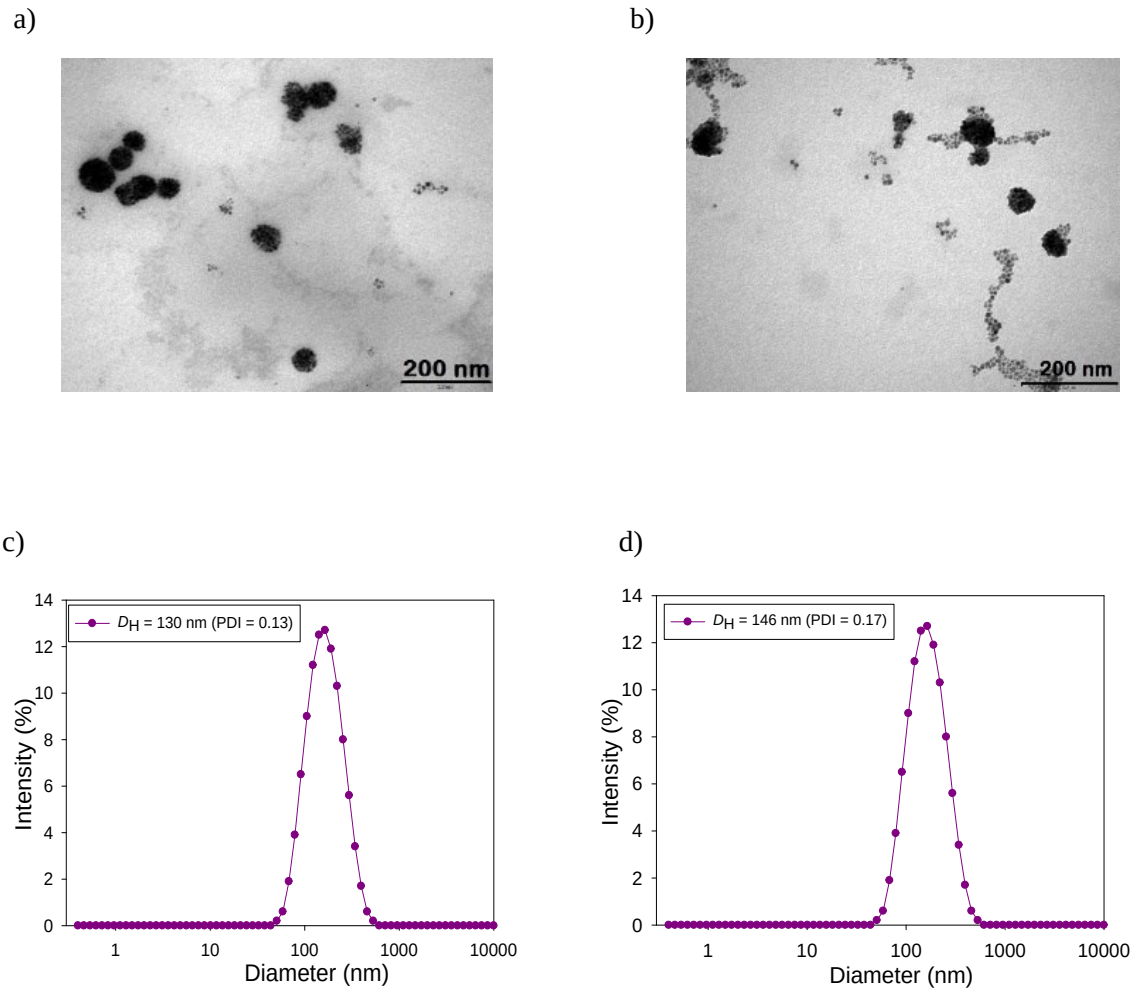

Figure S11. TEM images (a and b) and intensity-weighted size distributions (c and d) of PEO_{45}-*b*-PCL_{111} vesicles loaded at 16% FWR with 7.6 nm iron oxide nanoparticles: a) and c) sample left 7 days at 37°C and at pH 7 and b) and d) sample left 7 days at 37°C and at pH 5.

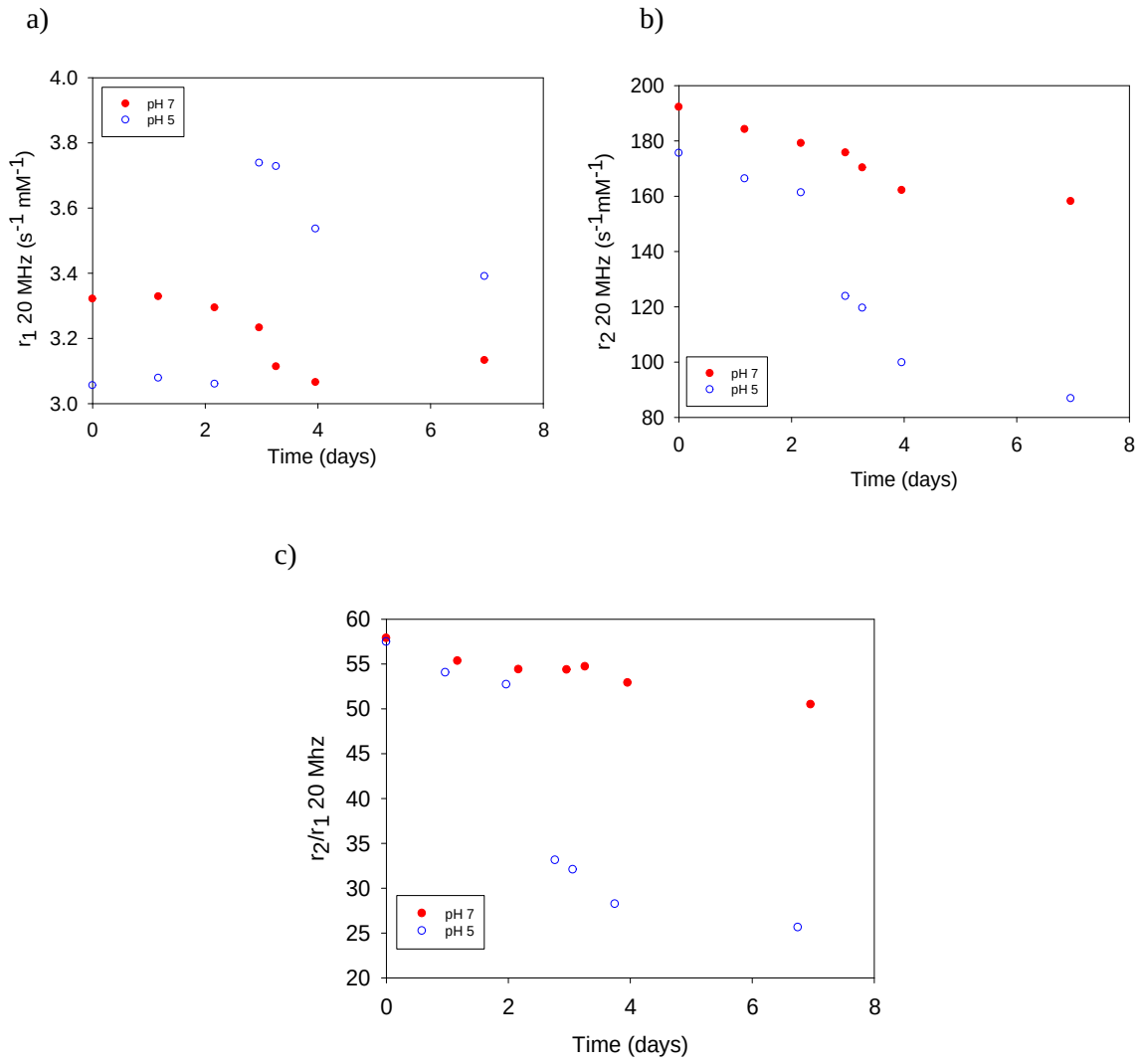

Figure S12. Longitudinal relaxivities (a), transverse relaxivities (b) and transverse to longitudinal relaxivity ratios (c) at 20 MHz for PEO_{45}-*b*-PCL_{111} vesicles loaded at 16% FWR with 7.6 nm USPIOs at pH 7 (red markers) and pH 5 (blue markers) as function of time.